Abelian math xmlns="http://www.w3.org/1998/Math/MathML">mrow>msub>mrow>mi>SU/mi>mo>(/mo>mi>N/mi>mo>)/mo>/mrow>mn>1/mn>/msub>/mrow>/math> chiral spin liquids on the square lattice

Ji-Yao Chen, Jheng-Wei Li, Pierre Nataf, Sylvain Capponi, Matthieu Mambrini, Keisuke Totsuka, Hong-Hao Tu, Andreas Weichselbaum, Jan von Delft, and Didier Poilblanc

Abelian $\mathrm{SU}(N)_1$ Chiral Spin Liquids on the Square Lattice

Ji-Yao Chen,[1,2] Jheng-Wei Li,[3] Pierre Nataf,[4] Sylvain Capponi,[5] Matthieu Mambrini,[5] Keisuke Totsuka,[6] Hong-Hao Tu,[7] Andreas Weichselbaum,[8] Jan von Delft,[3] and Didier Poilblanc[5]

[1]*Max-Planck-Institut für Quantenoptik, Hans-Kopfermann-Straße 1, 85748 Garching, Germany*
[2]*Munich Center for Quantum Science and Technology, Schellingstraße 4, 80799 München, Germany*
[3]*Arnold Sommerfeld Center for Theoretical Physics, Center for NanoScience, and Munich Center for Quantum Science and Technology, Ludwig-Maximilians-Universität München, 80333 Munich, Germany*
[4]*Laboratoire de Physique et de Modélisation des Milieux Condensés,*
Maison des Magistères, CNRS, 25 avenue des Martyrs, BP166, 38042 Grenoble, France
[5]*Laboratoire de Physique Théorique, Fédération Fermi,*
Université de Toulouse, CNRS, UPS, 31062 Toulouse, France
[6]*Yukawa Institute for Theoretical Physics, Kyoto University, Kitashirakawa Oiwake-Cho, Kyoto 606-8502, Japan*
[7]*Institut für Theoretische Physik, Technische Universität Dresden, 01062 Dresden, Germany*
[8]*Condensed Matter Physics and Materials Science Department,*
Brookhaven National Laboratory, Upton, New York 11973, USA
(Dated: October 12, 2021)

In the physics of the Fractional Quantum Hall (FQH) effect, a zoo of Abelian topological phases can be obtained by varying the magnetic field. Aiming to reach the same phenomenology in spin-like systems, we propose a family of $\mathrm{SU}(N)$-symmetric models in the fundamental representation, on the square lattice with short-range interactions restricted to triangular units, a natural generalization for arbitrary N of an SU(3) model studied previously where time-reversal symmetry is broken explicitly. Guided by the recent discovery of $\mathrm{SU}(2)_1$ and $\mathrm{SU}(3)_1$ chiral spin liquids (CSL) on similar models we search for topological $\mathrm{SU}(N)_1$ CSL in some range of the Hamiltonian parameters via a combination of complementary numerical methods such as exact diagonalizations (ED), infinite density matrix renormalization group (iDMRG) and infinite Projected Entangled Pair State (iPEPS). Extensive ED on small (periodic and open) clusters up to $N = 10$ and an innovative $\mathrm{SU}(N)$-symmetric version of iDMRG to compute entanglement spectra on (infinitely-long) cylinders in all topological sectors provide unambiguous signatures of the $\mathrm{SU}(N)_1$ character of the chiral liquids. An SU(4)-symmetric chiral PEPS, constructed in a manner similar to its SU(2) and SU(3) analogs, is shown to give a good variational ansatz of the $N = 4$ ground state, with chiral edge modes originating from the PEPS holographic bulk-edge correspondence. Finally, we discuss the possible observation of such Abelian CSL in ultracold atom setups where the possibility of varying N provides a tuning parameter similar to the magnetic field in the physics of the FQH effect.

I. INTRODUCTION

Quantum spin liquids are states of matter of two-dimensional electronic spin systems not showing any sign of spontaneous symmetry breaking down to zero temperature [1–3]. Spin liquids with long-range entanglement may also exhibit topological order [4] such as the spin-1/2 Resonating Valence Bond (RVB) state on the Kagome lattice [5]. Among the broad family of spin liquids, chiral spin liquids (CSL) [6–10] form a very special and interesting class [11] exhibiting broken time-reversal symmetry and chiral topological order [4]. Intimately related to FQH states [12], CSL are incompressible quantum fluids (i.e. with a bulk gap) and host both (Abelian or non-Abelian) anyonic quasi-particles in the bulk [13] and chiral gapless modes on the edge [14]. After the original papers, the Kalmeyer-Laughlin CSL lay dormant for many years until an explicit parent Hamiltonian was constructed [15, 16] using Laughlin's idea [8]. Later somewhat simpler Hamiltonians were found using different methods [17, 18]. An important step towards the goal of finding a chiral spin liquid in realistic systems was taken by examining a physically motivated model for a Mott insulator (Hubbard model) with broken time-reversal symmetry [19, 20]. Then, an Abelian CSL was identified in the (chiral) spin-1/2 Heisenberg model on the triangular lattice [21, 22]. Note that CSL hosting non-Abelian excitations (useful for topological quantum computing [23])

have also been introduced in different contexts [24–26].

It was early suggested that, in systems with enhanced $\mathrm{SU}(N)$ symmetry, realizable with ultracold alkaline earth atoms loaded in optical lattices [27], CSL can naturally appear [28], although this original proposal on the square lattice remained controversial. Later on, an Abelian CSL was indeed identified on the triangular lattice in $\mathrm{SU}(N)$ Heisenberg models with $N > 2$ [29]. The presence of a chiral spin interaction, achievable experimentally via a synthetic gauge field, seems to be a key feature to stabilize $\mathrm{SU}(N)$ CSL [30]. Nevertheless, the T and P violation required for a CSL could emerge spontaneously in T-invariant models, as found for $N = 2$ in a spin-1/2 Kagome Heisenberg model [31–33] or, for $N = 3$, in the Mott phase of a Hubbard model on the triangular lattice [34]. Note also that, using optical pumping, it is now possible to realize (so far in one dimension) strongly correlated liquids of ultracold fermions with a tunable number N of spin components and $\mathrm{SU}(N)$ symmetry [35]. This offers the prospect to be able to experimentally tune the system through various topological liquids, as it is realized in the physics of the FQH effect via a tunable external magnetic field. Apart from ultracold atom setups, condensed matter systems may also host $\mathrm{SU}(N)$ CSL. For example, it has been proposed very recently that an SU(4) CSL could be realized in double-layer moiré superlattices [36].

In recent years, Projected Entangled Pair States (PEPS) [37]

have progressively emerged as a powerful tool to study quantum spin liquids providing variational ground states competitive with other methods [38–40]. PEPS also offer a powerful framework to encode topological order [41–43] and construct chiral Abelian [44] and non-Abelian [45] SU(2) spin liquids. Generically, SU(2) CSL described by PEPS exhibit linearly dispersing chiral branches in the entanglement spectrum (ES) well described by Wess-Zumino-Witten (WZW) $\mathrm{SU(2)}_k$ (with the level of the WZW model $k = 1$ for Abelian CSL) conformal field theory (CFT) for one-dimensional edges [46].

Recently, on a square lattice with three-dimensional spin degrees of freedom which transform as the fundamental representation of SU(3) on every site, an Abelian CSL was found as the ground state (GS) of a simple Hamiltonian involving only nearest-neighbor and next-nearest-neighbor (color) permutations and (imaginary) three-site cyclic permutations [47]. Exact diagonalizations (ED) of open finite-size clusters and infinite-PEPS (iPEPS) in the thermodynamic limit (and encoding the full SU(3) symmetry) unambiguously showed the existence of chiral edge modes following the $\mathrm{SU(3)}_1$ WZW CFT. Interestingly, these results can be viewed as extending previous results obtained for an SU(2) spin-1/2 (i.e. $N = 2$) chiral Heisenberg model [20, 48]. Exactly the same type of Hamiltonian can be defined for N-dimensional spin degrees of freedom transforming according to the fundamental representation of SU(N), for arbitrary integer $N \geq 2$. It is then natural to speculate that, if such SU(N) models also host CSLs for $N > 3$, then the later should also be of the SU(N)$_1$ type. Note however that, although a chiral perturbation necessary induces, from linear response theory, a finite response of the quantum spin system, it, by no means, implies the existence of topological order or the absence of conventional (lattice or magnetic) symmetry breaking, which both characterize a CSL. The emergence of a uniform CSL with protected edge modes is therefore a subtle feature that needs to be investigated on a case by case basis. It is far from clear that the findings for SU(3) generalize to SU($N > 3$) bearing in mind that N may be commensurate or incommensurate with the fixed number of nearest neighbors on the square lattice. Then, in this work, we have (i) generalized the chiral Hamiltonians of Refs. [20, 47, 48] to arbitrary N, (ii) defined a subset of these SU(N) models whose Hamiltonians can be written solely as a sum of S_3-symmetric operators acting on all triangles within square plaquettes (as in Ref. [47]) and (iii) studied these models up to $N = 10$ using a combination of complementary numerical techniques such as ED, Density Matrix Renormalization Group (DMRG) and iPEPS, supplemented by CFT analytical predictions.

We then start by generalizing the SU(2) and SU(3) chiral Hamiltonians by placing, on every site of a square lattice, an N-dimensional spin degree of freedom, which transforms as the fundamental representation of SU(N). As for $N = 3$, we consider the most general SU(N)-symmetric short-range three-site interaction:

$$H = J_1 \sum_{\langle i,j \rangle} P_{ij} + J_2 \sum_{\langle\langle k,l \rangle\rangle} P_{kl} \qquad (1)$$

$$+ J_R \sum_{\triangle ijk} (P_{ijk} + P_{ijk}^{-1}) + iJ_\mathrm{I} \sum_{\triangle ijk} (P_{ijk} - P_{ijk}^{-1}),$$

where the first (second) term corresponds to two-site permutations over all (next-)nearest-neighbor bonds, and the third and fourth terms are three-site (clockwise) permutations on all triangles of every plaquette. P_{ij} (P_{ijk}) is defined through its action on the local basis states, $P_{ij}|\alpha\rangle_i|\beta\rangle_j = |\beta\rangle_i|\alpha\rangle_j$ ($P_{ijk}|\alpha\rangle_i|\beta\rangle_j|\gamma\rangle_k = |\gamma\rangle_i|\alpha\rangle_j|\beta\rangle_k$, for a fixed orientation of the triangle i, j, k, let say anticlockwise). To restrict the number of parameters we have chosen $J_2 = J_1/2$. In that case, the two-body part (J_1 and J_2) on the interacting triangular units becomes S_3 symmetric, hence mimicking the corresponding Hamiltonian on the triangular lattice [49]. We then use the same parametrization as in Ref. [47]:

$$\begin{aligned}
J_1 = 2J_2 &= \tfrac{4}{3}\cos\theta\sin\phi, \\
J_R &= \cos\theta\cos\phi, \qquad (2)\\
J_\mathrm{I} &= \sin\theta,
\end{aligned}$$

and restrict ourselves to *antiferromagnetic* couplings $J_1, J_2 > 0$, i.e. $0 \leq \theta \leq \pi/2$ and $0 \leq \phi \leq \pi$. Note however that, for $\phi > \pi/2$, the amplitude of the (real) 3-site permutation J_R becomes ferromagnetic ($J_R < 0$). A detailed analysis of the multiplet structure of a 2×2 plaquette of the Hamiltonian above is given in App. A.

For $N = 2$, various forms of the Hamiltonian (1) can be found in the literature [20, 48]. In the original formulation [20], a chiral interaction $4J_3\, \mathbf{S}_i \cdot (\mathbf{S}_j \times \mathbf{S}_k)$ on all triangular units $\triangle(ijk)$ is introduced, corresponding to the 3-site cyclic permutations of (1) with amplitudes $J_R = 0$ and $J_\mathrm{I} = J_3$. Also, the 2-site exchange interactions are introduced here as spin-1/2 Heisenberg couplings, which is equivalent from the identity $2\mathbf{S}_i \cdot \mathbf{S}_j = P_{ij} - \frac{1}{2}$ [50]. A Hamiltonian including a (pure-imaginary) cyclic permutation $i\lambda_c(P_{ijkl} - P_{ijkl}^{-1})$ on each plaquette $\square(ijkl)$ was also introduced [48]. In fact, the plaquette cyclic permutation $i(P_{ijkl} - \mathrm{h.c.})$ can be rewritten as $\frac{i}{2}(P_{ijk} + P_{jkl} + P_{kli} + P_{lij} - \mathrm{h.c.})$ [51] so that this model corresponds also to $J_R = 0$ and we can identify $J_\mathrm{I} = J_3 = \lambda_c/2$. An optimum choice of parameters for the stability of the SU(2) CSL phase is found to be (in our notations) $J_2/J_1 \simeq 0.47$ and $J_\mathrm{I}/J_1 \simeq 0.21$ [20]. Furthermore, evidence is provided that the CSL survives in a rather extended zone of parameter space around this point. Also, an SU(2)-symmetric PEPS ansatz [44] provides an accurate representation of the GS at the optimum values of the parameters [48], and of its edge modes [52] following an SU(2)$_1$ WZW CFT.

For $N = 3$, from ED, DMRG and iPEPS simulations, clear evidence of a gapped CSL is found for $J_2 = J_1/2$ and angles like $\theta = \phi = \pi/4$ corresponding to $J_R/J_1 = 0.75$ and $J_\mathrm{I}/J_1 \simeq 1.06$ [47], and around these values in a rather extended parameter range (see Supplemental Materials of Ref. [47]). In addition, edge modes are found to closely follow the predictions of the SU(3)$_1$ CFT.

In the following, we will investigate model (1) using complementary ED and DMRG techniques, providing overwhelming evidence of a stable topological CSL phase. Various systems of different topology, as shown in Fig. 1, will
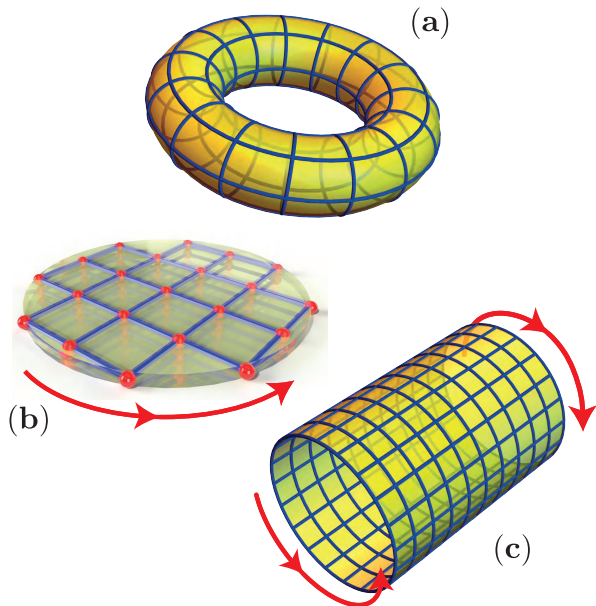
N_s	$\mathbf{t}_1$	$\mathbf{t}_2$	point group
8	$(2,2)$	$(2,-2)$	C_{4v}
11	$(1,3)$	$(3,-2)$	C_2
12	$(1,3)$	$(4,0)$	C_2
13	$(2,-3)$	$(3,2)$	C_4
14	$(1,4)$	$(3,-2)$	C_2
15	$(1,4)$	$(4,1)$	C_{2v}
16	$(4,0)$	$(0,4)$	C_{4v}
18	$(3,3)$	$(3,-3)$	C_{4v}
19	$(1,4)$	$(4,-3)$	C_2
20	$(4,2)$	$(-2,4)$	C_4
21	$(1,4)$	$(5,-1)$	C_2

TABLE I. List of periodic clusters used here in ED: number of sites N_s, cluster size vectors $\mathbf{t}_1$ and $\mathbf{t}_2$, and point-group symmetry. Eigenstates can be labeled according to discrete momenta in the BZ. At high-symmetry points Γ, X or M of the BZ, eigenstates can be further labeled by the C_4-symmetry (C_2-symmetry) IRREP labels, A, B, E_a and E_b (A and B) – see Fig. 4.

FIG. 1. We considered various system topologies: **(a)** periodic cluster topologically equivalent to a torus; **(b)** open cluster topologically equivalent to a disk; **(c)** cylinder with left and right boundaries. We used **(a)** and **(b)** in ED and the infinite-length version of **(c)** in DMRG and iPEPS. The chiral modes of the CSL are schematically shown on the system edges.

be used. A torus geometry enables to probe bulk properties while a disk or a cylinder geometry, with one or two edges respectively, provides information on the existence and on the nature of edge modes. More precisely, the topological nature of a CSL phase can be established from (i) the topological GS degeneracy [4] on periodic clusters, (ii) the existence of chiral edge modes [14] both in open systems like Figs. 1(b) and in the entanglement spectra of (quasi-)infinite cylinders, and (iii) the content of the edge modes following closely the prediction of some chiral CFT theory. The Abelian CSL expected here should be revealed by exactly N quasi-degenerate GS on a closed manifold and by the exact $SU(N)_1$ WZW CFT content of its edge modes. The second goal of the paper, beside establishing the existence of the $SU(N)_1$ CSL phase itself, is to provide its faithful representation in terms of an $SU(N)$-symmetric PEPS. Following the prescription for $N = 2$ and $N = 3$, we shall focus on the $N = 4$ case. Common features observed for PEPS with these three values of N allow us to draw heuristic rules and conclusions for general N.

II. EXACT DIAGONALIZATIONS

A. Exact diagonalizations in the U(1) basis and in the standard Young tableaux (SYT) basis

We start this section by a brief review of the two distinct and complementary exact diagonalisation methods used in this work.

First, for periodic clusters (see Table I), we can implement the spatial symmetries (and in particular the translations) which allows us to both reduce the size of the matrix to diagonalize by a factor typically equal to N_s (where N_s is the size of the cluster) and to directly obtain the momenta associated to each eigenenergy.

However, as N increases, EDs performed this way are severely limited by the size of the available clusters since the dimension of the Hilbert space increases exponentially with N_s. A way to overcome such limitations is to implement the $SU(N)$ symmetry and this is the second ED protocol that we have employed here. In particular, when N_s is a multiple of N, the ground state of Hamiltonian (1) is an $SU(N)$ singlet state for a wide range of parameters. The singlet sector has a dimension much smaller than the one of the full Hilbert space. The gain to implement the full $SU(N)$ symmetry and to look for the lowest energy states directly in the singlet sector is huge and increases with N. For instance, for $N = 10$ and $N_s = 20$, the singlet sector has only dimension 16796, while the dimension of the full Hilbert space is 10^{20}. In addition, to write the matrix representing the Hamiltonian in the singlet subspace and in the sectors labeled by higher dimensional $SU(N)$ irreducible representation (IRREP), we have employed the algorithms detailed in Refs. [53, 54], which is mainly based on the use of Standard Young Tableaux and on the theory of the representation of the permutation group.

In particular, it allows one to bypass the need for the Clebsch-Gordan coefficients, which can only be calculated with an algorithm whose complexity also increases with N (see Ref. [55]). Typically, for the present problem, through this method, we can address clusters with $N_s \sim 20$ sites for N up to 10. Note that contrary to the first ED method based on the implementation of spatial symmetries, the momenta can only be accessed in a second stage: we first calculate the eigenvectors and then the effect of translation or rotation on them.
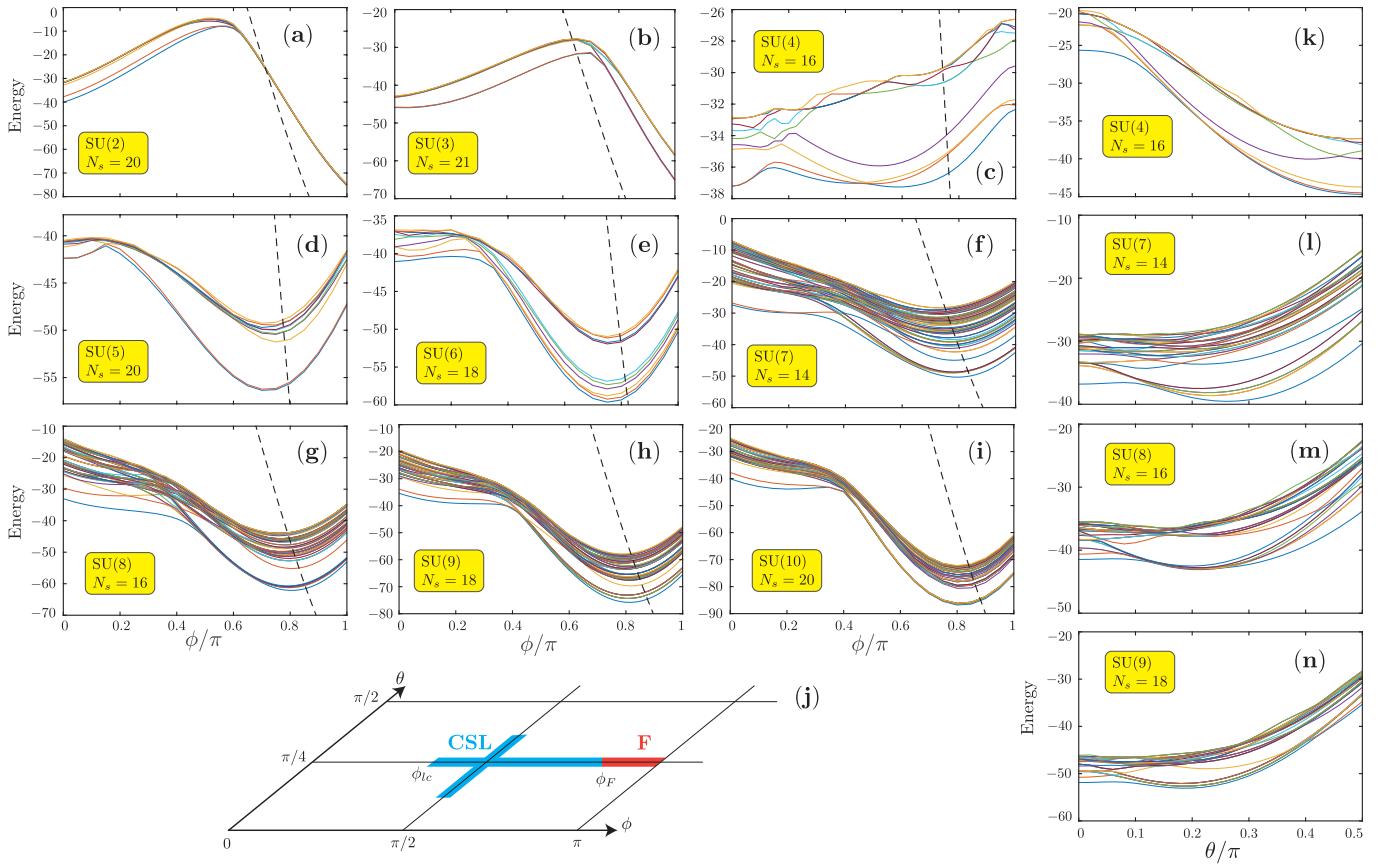
FIG. 2. Low energy spectra computed by ED in the SYT singlet basis on periodic clusters of $N_s = kN$ sites, $k \in \mathbb{N}$, and **(a-i)** for a fixed value of $\theta = \pi/4$ as a function of ϕ, for N ranging from 2 to 10, or **(k-n)** for a fixed value of $\phi = \pi/2$ as a function of $\theta \in [0, \pi/2]$, for $N = 4, 7, 8, 9$. Only 10 (40) lowest singlet levels are shown at small N in **(a-e)** and **(k)** (larger N in **(f-i)** and **(l-n)**). The ϕ and θ axis being discretized, lines connecting the data points are used as guides to the eye (hence, levels crossings around $\phi_{\rm lc}$ may look like anti-crossings). N degenerate or quasi-degenerate singlets (see Figs. 3,4 and text) are separated from the higher energy states by a gap, in an extended (ϕ, θ) region around $(\pi/2, \pi/4)$. The energy of the (fully polarized) ferromagnetic state ($E_{\rm ferro} = 2\sqrt{2}N_s(2\cos\phi + \sin\phi)$), crossing the singlet GS at $\phi = \phi_F$, is shown as a dashed line in **(a-i)**. The location of the CSL and ferromagnetic phases along the cuts **(c-i)** and **(k-n)** are schematized in **(j)**. Note that for $N = 2, 3$ **(a,b)** the CSL is expected to extend all the way to $\phi = 0$.
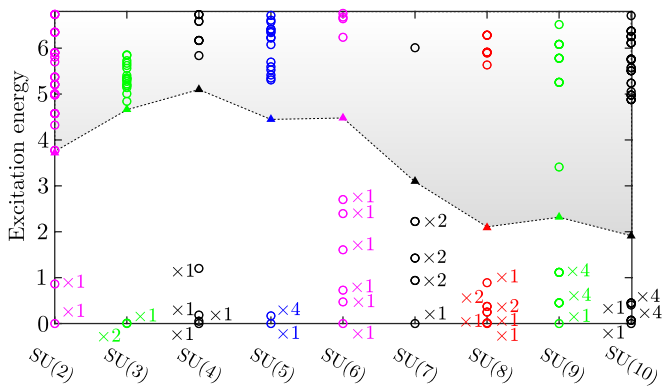
FIG. 3. Zoom of the singlet low-energy spectra at $\theta = \pi/4$ and $\phi = \pi/2$, for N ranging from 2 to 10, and the same cluster sizes as in Fig. 2. The GS energy is subtracted off for better comparison between the various spectra. The exact degeneracy g of each level is indicated on the plot as $\times g$. The first non-singlet excitation belonging to the adjoint IRREP above the N quasi-degenerate low-energy singlets is shown as a filled triangle (see text).

B. Periodic clusters : bulk gap and GS manifold

The results for $N = 2$ and $N = 3$ described above suggest that the existence of an Abelian CSL may be generic for arbitrary integer N. To investigate such an appealing scenario, we start by examining, for larger N, the low-energy spectra obtained on N_s-site periodic clusters (see Table I for details about clusters used). For antiferromagnetic and frustrating couplings $J_1 > 0$, $J_2 > 0$, we expect the lowest-energy to belong to the antisymmetric IRREP $\mathrm{aIR}_N(r_0)$ defined by a Young tableau of r_0 vertical boxes, $r_0 = \mathrm{mod}(N_s, N)$. In particular, in the case where N_s is an integer multiple of N ($r_0 = 0$), the low-energy states are expected to belong to the singlet subspace. However, at e.g. $\theta = \pi/4$, when increasing ϕ beyond $\phi = \pi/2$, J_R changes sign and states belonging to the antisymmetric IRREP are gradually destabilized with respect to the completely symmetric (ferromagnetic) state of energy $E_{\rm ferro}/N_s = 3J_1 + 8J_R$. In particular, we clearly see at $\theta = \pi/4$ a *macroscopic* energy gain (penalty) of the lowest-energy eigenstate of $\mathrm{aIR}_N(r_0)$ with respect to the fer-
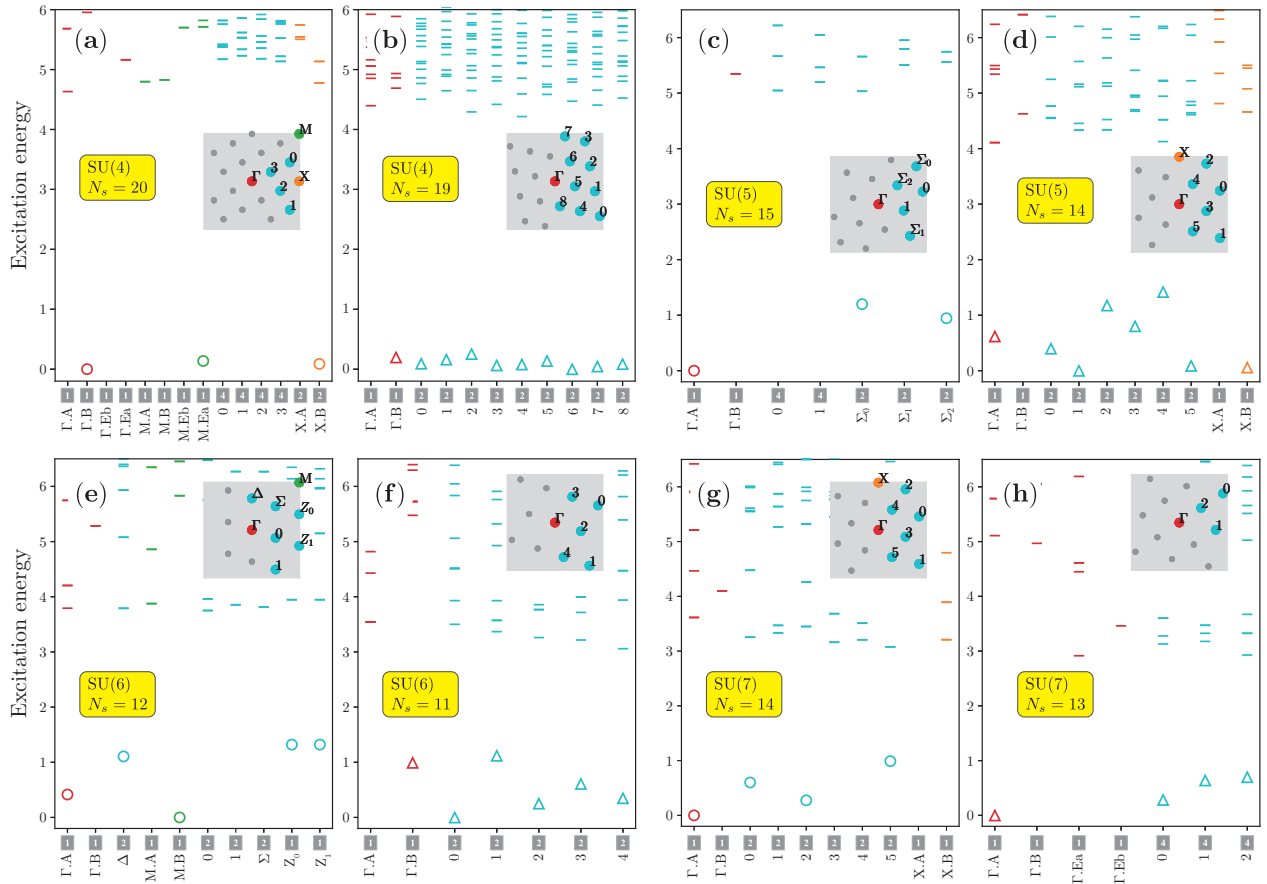
FIG. 4. Low-energy spectra on periodic clusters at fixed $\phi = \pi/2$ and for $\theta = \pi/4$ **(a-d)** or $\theta = \pi/6$ **(e-h)**. Clusters with site numbers $N_s = kN$ (left) or $N_s = kN - 1$ (right), $k \in \mathbb{N}$, are chosen to obtain 0 and 1 quasi-hole, respectively, in the putative CSL. The respective BZ with the allowed discrete momenta is shown on each plot as a gray square – only non-equivalent momenta are labeled – and the number of equivalent momenta appearing are listed as grayed squared numbers. For $N_s = kN$ (left), the GS manifold is composed of N singlets (open circles). For $N_s = kN - 1$ (right), it is composed of N_s quasi-degenerate levels, one level at each cluster momentum. Each level is comprised of N degenerate states forming a $\bar{N}$ anti-fundamental IRREP (open triangles).

romagnetic state at $\phi = \pi/2$ ($\phi = \pi$) (see App. D). This fact indicates a transition at $\phi = \phi_F$ (somewhere in the range $\pi/2 < \phi_F < \pi$) between one (or several) spin liquid phase(s) and a ferromagnetic phase. Note also that a detailed analysis of the 2×2 plaquette Hamiltonian in App. A, shows that the antiferromagnetic states dominate the low energy regime, yet with the ferromagnetic regime in close proximity.

We now focus on the prospective spin liquid region discussed above and consider the case of $N_s = kN$, $k \in \mathbb{N}$, so that no quasiparticle excitations would be populating the GS of a CSL phase. To identify the exact nature(s) of the spin liquid(s), one needs to examin in details the low-energy singlet subspace (gap structure, degeneracies, etc...). A selection of the singlet energy spectra for fixed $\theta = \pi/4$, plotted versus ϕ (for fixed $\phi = \pi/2$, plotted versus θ), is shown in Fig. 2 for N ranging from 2 to 10 (for $N = 4, 7, 8, 9$). For all the values of N studied here, in a broad interval of ϕ ($\phi < \phi_F$) or θ values, a clear gap is observed between a group of degenerate and quasi-degenerate states and the rest of the singlet spectrum. Interestingly, for $\theta = \pi/4$ and $N > 3$, we observe level crossings occuring in the singlet subspace at some value of

$\phi_{lc} < \pi/2$, suggesting the existence of two different gapped phases. For $0 \le \phi < \phi_{lc}$, we observe a two-fold quasi-degenerate GS manifold within the singlet subspace which are translationally invariant but which break the lattice point group $\pi/2$-rotation symmetry [56]. This could correspond to a nematic valence cluster state as also seen in SU(2) spin-1 models [57, 58]. Note that, as a finite-size effect, the ground state of the total spectrum for small ϕ and θ around $\pi/4$ is not necessarily a singlet state when $N_s < N^2$ (see App. D). A more careful investigation of this phase, although interesting, is beyond the scope of this work and left for a future study.

We now move to a closer inspection of the gapped spin liquid phase seen for $N = 2, 3$ and $\phi < \phi_F$, and for $N > 3$ and $\phi_{lc} < \phi < \phi_F$, and identify it as a CSL. Interestingly, we note that $\phi = \pi/2$ – corresponding to a pure imaginary 3-site cyclic permutation – is always located within this gapped phase (Note, for $N = 3$, $\phi = \pi/4$ instead was chosen in Ref. [47]). This gapped phase is also stable within a significant range of the parameter θ, around $\theta = \pi/4$ and $\phi = \pi/2$, e.g. also at $\theta = \pi/6$. Hence, in the following, we shall mostly report results obtained at fixed $\phi = \pi/2$ (i.e. for a pure imag-
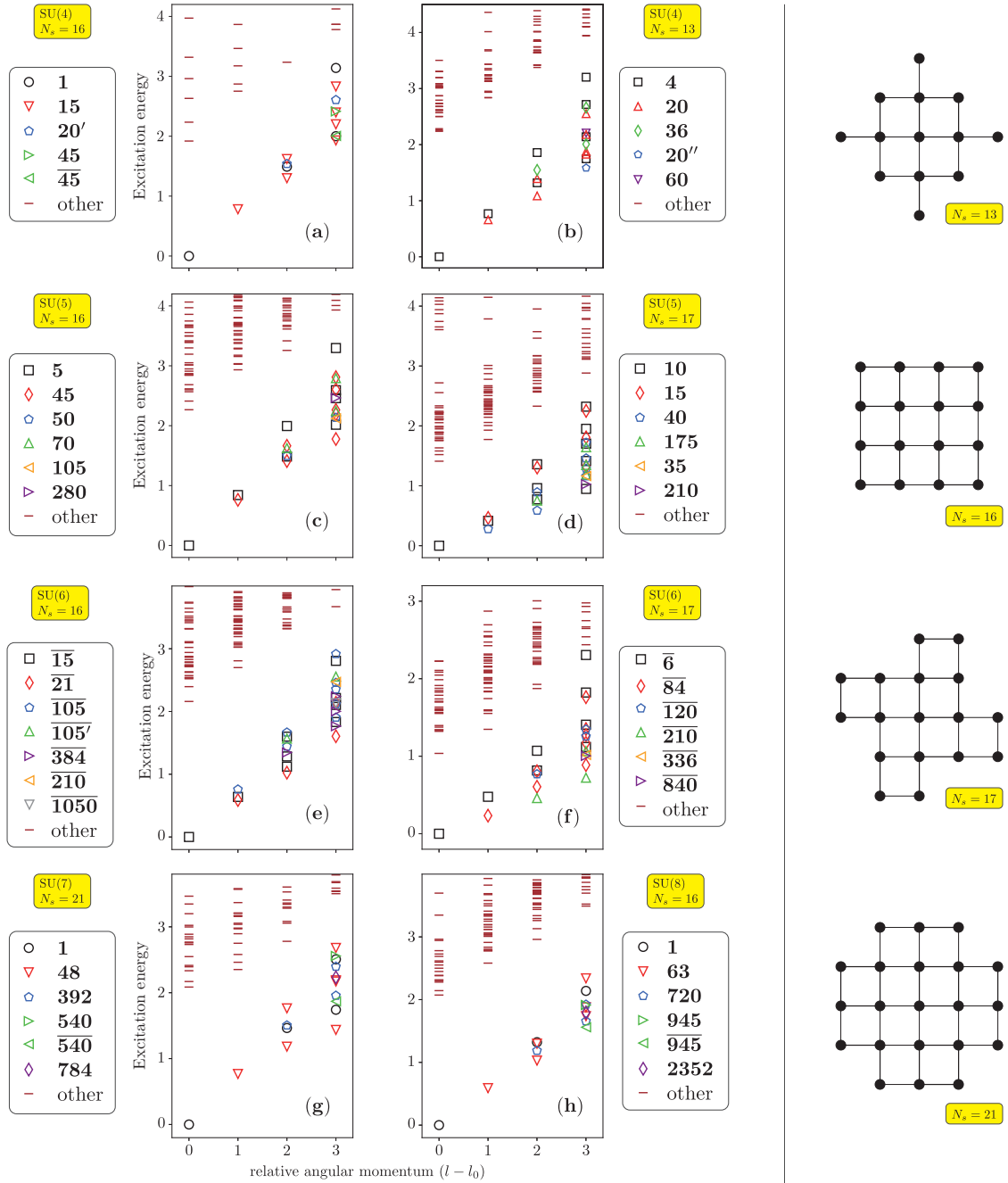
FIG. 5. Low-energy spectra on open C_4-symmetric clusters depicted on the right-hand side of the figure, as a function of the angular momentum l (with respect to the GS angular momentum l_0), at fixed $\phi = \pi/2$ and for $\theta = \pi/4$ (a-d) or $\theta = \pi/6$ (e-h). Symbols labeling the various SU(N) IRREPs entering the chiral mode are shown in the legends. The Young diagrams for the corresponding IRREPs can be identified using the tables in App. C. The GS IRREPs are fully antisymmetric, and labeled by Young diagrams consisting of a single column of $r_0 = \mathrm{mod}(N_s, N)$ boxes, with degeneracy $\frac{N!}{(N-r_0)!r_0!}$. Identifying $l - l_0$ with the Virasoro level L_0, all low-energy ToS in (a-h) for $0 \leq l - l_0 \leq 3$ follow exactly the WZW CFT predictions of Tables VIII,IX,XII,XIII,XVI,XV,XVII and XXI, respectively. The only exception is the SU(6) $\overline{15}$ (SU(8) $\mathbf{1}$) tower, for which two multiplets $\overline{15}$ and $\overline{21}$ ($\mathbf{1}$ and $\overline{63}$) are missing in the $L_0 = 3$ Virasoro level.

inary 3-site permutation) and for $\theta = \pi/4$ or, occasionally, $\theta = \pi/6$.

To identify the type of (singlet) gapped phase, we now investigate the exact degeneracy and the quantum numbers of the singlet GS manifold. Fig. 3 shows a zoom of the low-

energy spectra at $\theta = \pi/4$ and $\phi = \pi/2$, with the exact degeneracy of each level below the gap. A simple counting shows that there are exactly N states below the gap. Note that the first excitation defining the gap does not belong to the singlet sector but most often belongs to the adjoint IR-

REP of dimension $N^2 - 1$, except for some of the largest values of N (like $N = 9$) for which finite size effects are the strongest. This is an extension of the SU(2) case where the first excitation in antiferromagnetic spin liquids are typically spin-1 "magnons". In the thermodynamic limit, the gap in the singlet sector should be bounded from above by twice the true "magnetic" gap as two isolated "magnons" can fuse into a singlet. If a singlet bound state occurs between two magnons, the singlet gap is then strictly smaller than twice the magnon gap.

The above observation of the N-fold degeneracy of the GS space suggests that the gapped phases indeed correspond to Abelian SU(N)$_1$ chiral spin liquids. As realized already for $N = 3$ in Ref. [47], it is possible to obtain, for arbitrary N, the exact momenta of the various states in the GS manifold expected for an Abelian SU(N)$_1$ CSL. This can be inferred from a simple generalized exclusion principle (GEP) [59, 60] with clustering rules (see App. B for details). As a final check for periodic systems, we then focus on two distinct commensurability relations between the cluster size N_s and N; either, (i) $N_s = kN$, $k \in \mathbb{N}$, for which, as above, the GS contains no quasi-particle and (ii) $N_s = kN - 1$, $k \in \mathbb{N}$, for which, a single quasi-hole populates the GS. Note that in case (ii), $r_0 = N - 1$ so that the IRREP of the GS manifold is the $\bar{N}$ anti-fundamental IRREP. The GEP implies a GS (quasi-)degeneracy of N and N_s for (i) and (ii), respectively. This is indeed observed as shown in Fig. 4. The predictions of the GEP are even more precise, providing all GS momenta expected for the (Abelian) CSL on every periodic cluster (see App. B for details on the way momenta are assigned). We have checked that – in most cases – all GS momenta reported in Fig. 4 match the ones predicted by the heuristic rules. In particular, for $N_s = kN - 1$, the GS manifold is made of exactly one $\bar{N}$ (antifundamental) IRREP at each cluster momentum. Rare failures of the GEP rules (which may be attributed to cluster shapes, etc. . .) to predict the correct momenta will be discussed in App. B.

Interestingly, the above features predicted and observed in the case of a single quasi-hole can be understood using a simple physical argument. If the single quasi-hole would be static, it could be placed on each of the N_s sites of the cluster, and this, for each of the N topological (singlet) sectors, hence spanning a $N_s N$-dimensional Hilbert space. The effective hopping allows the quasi-hole states to form a weakly dispersing band below the gap, hence with N states at every momentum. From the SU(N)-symmetry, these N states should form a single multiplet belonging to the $\bar{N}$ (antifundamental) IRREP, as predicted by the GEP and found numerically.

C. Open systems : edge physics and CFT content

The previous results give strong evidence of the CSL nature of the GS of the model, for the parameters chosen, from its bulk properties on periodic systems (topologically equivalent to tori). We complete the identification of the CSL phase by the investigation by ED of open clusters. The existence of a chiral edge mode fulfilling the SU(N)$_1$ WZW CFT should be reflected in the precise content of its low-energy spectrum. By choosing finite-size clusters with (i) open boundaries and (ii) C_4 point-group symmetry, we can investigate the low-energy spectrum as a function of the angular momentum, $l = 0, \pm 1, 2$ (mod[4]) and reveal a single chiral branch linearly dispersing only in one direction, as expected. At a given N, changing the cluster size N_s – whenever such a C_4-symmetric cluster is available – enables to change the topological sector defined by the integer $r_0 = \text{mod}(N_s, N)$, $r_0 = 0, \cdots, N - 1$. Indeed, each topological sector is characterized by the SU(N) IRREP of its GS, corresponding to the antisymmetric IRREP aIR$_N(r_0)$ (defined by a Young tableau of r_0 vertical boxes), and can then be reached whenever $N_s = kN + r_0$. Note that the dimension of aIR$_N(r_0)$ is given by $\frac{N!}{(N-r_0)! r_0!}$.

The ED investigation of the chiral edge modes has been carried out on two types of open systems, all exhibiting C_4 symmetry with respect to the cluster center. The first type of clusters is build around a central site by adding successive shells of 4 sites at 90-degree angles. The second type of open clusters are built in the same way but from a center 2×2 plaquette. The 13-site, 17-site and 21-site (16-site) clusters belongs to the first (second) category, as shown on the right-hand side of Fig. 5. Note that the 17-site cluster is "chiral", i.e. it breaks reflection symmetry (parity), and spectra for $J_I > 0$ and $J_I < 0$ are expected to be (slightly) different. Here, $J_I > 0$ and the P_{ijk} permutation is assumed counterclockwise. ED spectra obtained on such clusters for $N = 4, 5, 6, 7, 8$ are shown in Fig. 5, for $\phi = \pi/2$ and $\theta = \pi/4$ or $\pi/6$ (as specified in the caption). In all cases, we observed a rather sharply-defined low-energy chiral edge mode, i.e. a group of levels (i) well-separated from higher-energy levels by a gap, (ii) following a linear dispersion with respect to the angular momentum and (iii) with a very precise and non-trivial content in terms of SU(N) multiplets. Each edge mode is characterized by its GS given by the antisymmetric IRREP aIR$_N(r_0)$. For each pair (N, r_0) occurring in Fig. 5, we have computed the expected "tower of states" (ToS) generated by aIR$_N(r_0)$, as predicted by the SU(N)$_1$ WZW CFT – see App. C. Numerically, one can use $(N - 1)$ $U(1)$ quantum numbers to diagonalize the Hamiltonian and identify the IRREP content for each group of *exactly* degenerate levels. A careful check shows that, generically, the quantum numbers of the chiral edge mode spectra match exactly the WZW CFT ToS predictions (identifying the angular momentum with the Virasoro level L_0), providing a real hallmark of the CSL phase. For two cases corresponding to the smallest $N_s = 16$ cluster, a small number of multiplets in the CFT predictions are missing in Fig. 5. We have explicitly checked that finite-size effects can indeed lead to incomplete towers.

III. DMRG

For characterizing chiral topological states, the correspondence between the entanglement spectrum and the conformal tower of states is a fingerprint evidence. While DMRG is in principle suited for this purpose, a technical difficulty is that the characterization of topological order requires the full set of (quasi-)degenerate ground states and, furthermore, these

states should be combined into the so-called minimally entangled state (MES) basis [61]. In this section, we use a two-step procedure to accomplish this task: i) build Gutzwiller projected parton wave functions which describe the $SU(N)_1$ CSL, use them to construct the MES basis on the cylinder, and convert them into MPS; ii) initialize DMRG with the parton-constructed MES basis. This strategy allows us to find the full set of N (quasi-)degenerate ground states in the MES basis. The parton picture also helps us to identify the correspondence between the entanglement spectrum and the $SU(N)_1$ conformal towers.

A. Parton wave functions

In this subsection, we outline the parton approach to construct trial wave functions for the $SU(N)$ CSL model. To construct the minimally entangled states (MESs) [61], we use a fermionic parton representation of the $SU(N)$ generators [62–64], $S_i^\mu = \sum_{\sigma\sigma'} c_{i\sigma}^\dagger T_{\sigma\sigma'}^\mu c_{i\sigma'}$, where $T_{\sigma\sigma'}^\mu$ are matrix representations of the $SU(N)$ generators in the fundamental representation, and $c_{i\sigma}^\dagger$ is the creation operator at site i. A local constraint $\sum_\sigma c_{i\sigma}^\dagger c_{i\sigma} = 1$ has to be imposed to ensure that singly-occupied fermions represent the N states in the $SU(N)$ fundamental representation, i.e., $|\sigma\rangle = c_\sigma^\dagger |0\rangle$ (site index suppressed), with $|0\rangle$ being the vacuum of partons. The $SU(N)$ CSL with $SU(N)_1$ topological order can be constructed by Gutzwiller projecting a fully occupied $C = 1$ Chern band of fermionic partons, where C is the Chern number. To have a systematic construction for all N, we design the following quadratic Hamiltonian for partons on a square lattice:

$$
\begin{aligned}
H_\mathrm{p} = &- \sum_{m,n,\sigma} \left(t_x c_{m+1,n,\sigma}^\dagger c_{m,n,\sigma} + t_y e^{im\varphi} c_{m,n+1,\sigma}^\dagger c_{m,n,\sigma} \right) \\
&- \sum_{m,n,\sigma} \left(t_2 e^{i(m\varphi \pm \pi/N)} c_{m\pm 1,n+1,\sigma}^\dagger c_{m,n,\sigma} \right) + \mathrm{h.c.} \\
&- \mu \sum_{m,n,\sigma} c_{m,n,\sigma}^\dagger c_{m,n,\sigma}.
\end{aligned}
\tag{3}
$$

The phase φ is chosen to be $2\pi/N$, so that the flux through each square plaquette is $2\pi/N$ and each triangular plaquette is π/N. To minimize finite-size effects, we maximize the band gap by choosing $t_2 = t_y/2$.

The design of the parton Hamiltonian (3) follows a lattice discretization of the Landau level problem, i.e., 2D electrons in a strong magnetic field (with the Landau gauge). Under periodic boundary conditions (torus geometry), the fluxes in the square/triangular plaquette are chosen such that there are N bands with the lowest band having Chern number $C = 1$ (see Fig. 6). The $N = 2$ case has been considered previously in Refs. [61, 65–67], which was used to constructed Gutzwiller projected wave functions representing the $SU(2)$ CSL of Kalmeyer-Laughlin type. For $N > 2$, the lowest band becomes flat and indeed resembles the lowest Landau level. The trial wave functions for describing the $SU(N)_1$
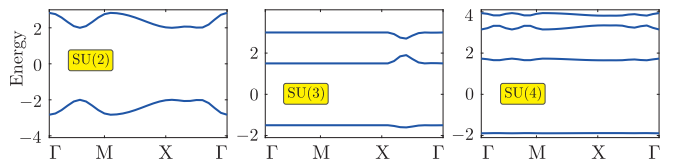
FIG. 6. Band structures of the parton Hamiltonian on the torus along high symmetry directions for $N = 2, 3$ and 4. We set $t_x = t_y$ for $N = 2$ and 4, and $t_x = t_y/2$ for $N = 3$.
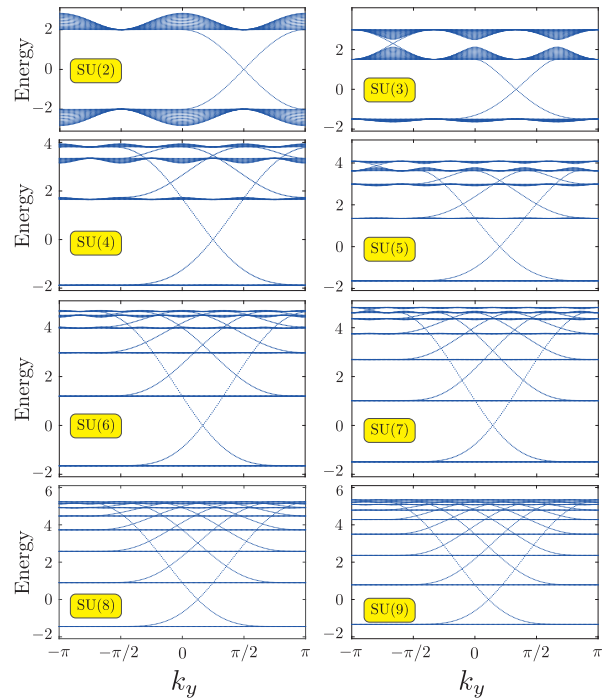
FIG. 7. The parton single-particle levels including the edge states on a wide cylinder for $N = 2$ to 9. Filling the Fermi sea up to zero energy corresponds to a filling fraction $1/N$. This fully occupies the lowest parton band as well as the edge states up to the degenerate zero modes at the single-particle momentum $k_y = \pi/N$. These exact zero modes, denoted by $d_{L\sigma}$ and $d_{R\sigma}$, are localized at the left and right boundaries of the cylinder, respectively.

CSL are obtained by (i) tuning the chemical potential μ such that the lowest band is completely filled and all others empty, yielding a filling of $1/N$ on the lattice when also including the edge mode (see Fig. 7) and (ii) Gutzwiller projecting the Fermi sea with fully occupied lowest band. Strictly speaking, this construction does not depend on the flatness of the $C = 1$ band. Here, our extra requirement of a nearly flat band serves another purpose: the single-particle wave functions of a flat band can be made more localized, which helps to suppress the entanglement growth when converting Gutzwiller projected wave functions into MPS [67]. Last but not the least, this parton Hamiltonian is also designed to support exact zero modes on the cylinder, which, as we shall see, are important for constructing the MES basis.

For our purpose, we shall consider the cylinder geometry (with circumference N_y) rather than the torus geometry, with
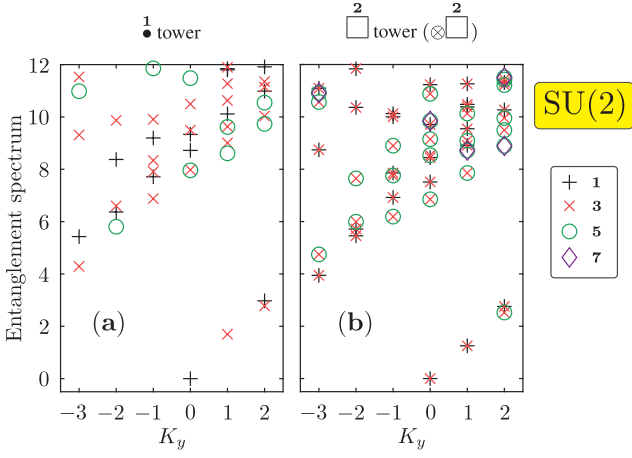
FIG. 8. The entanglement spectra on width-6 cylinders for SU(2) CSLs. **(a)** Identity sector. **(b)** Semion sector ($\otimes \frac{1}{2}$). Identifying K_y with the Virasoro level L_0, the content of the chiral branches agrees exactly with the CFT predictions of tables IV and II up to $K_y = 4$ (mod[6]).

TABLE II. $SU(2)_1$ WZW model – The direct product of the conformal tower of the spin-1/2 primary (left - see Table V in App. C) with a spin-1/2 gives a new tower (right) with a doubling of the number of states in each Virasoro level indexed by L_0.

open boundaries in the x direction and a periodic (or twisted) boundary condition in the y direction. This allows us to characterize the MESs via the entanglement spectrum [65, 68], and to use these wave functions to initialize our DMRG simulations [69].

By diagonalizing the parton Hamiltonian (3) on the cylinder, we obtain a set of single-particle orbitals composed of local operators, $d^\dagger_{k\sigma} = \sum_{m,n} A_{m,n}(k) c^\dagger_{m,n,\sigma}$. For $N = 2$, it is known that the exact zero modes play an important role in constructing the MESs [65, 67]. These exact zero modes, denoted by $d_{L\sigma}$ and $d_{R\sigma}$, localize at the two boundaries of the cylinder. Their occurrence at the single-particle momentum $k_y = \pi/2$ requires that for $\mathrm{mod}(N_y, 4) = 0$ (2), the parton Hamiltonian has periodic (antiperiodic) boundary condition in the y direction. The two MESs with $S_z = 0$ are then written as Gutzwiller projected wave functions, $|\Psi_1\rangle = P_G d^\dagger_{L\uparrow} d^\dagger_{R\downarrow} |\Phi\rangle$ and $|\Psi_2\rangle = P_G d^\dagger_{L\uparrow} d^\dagger_{L\downarrow} |\Phi\rangle$, where P_G imposes the single-occupancy constraint at each site and $|\Phi\rangle$ is the state with all

parton modes below the zero modes being fully occupied. In this representation, it is transparent that the zero mode $d^\dagger_{L(R)\sigma}$ creates a semion carrying spin-1/2 (with spin projection σ) at the left (right) boundary of the cylinder. It was found [67] that the entanglement spectra of $|\Psi_1\rangle$ and $|\Psi_2\rangle$ correspond to the conformal towers of states of the chiral $SU(2)_1$ WZW model in its spin-1/2 (semion) and spin-0 (identity) sectors, respectively. To qualify as the (quasi-) degenerate ground states of chiral spin liquids, the wave functions should be SU(2) spin singlets. While $|\Psi_2\rangle$ is manifestly a spin singlet, $|\Psi_1\rangle$ needs to be combined with $P_G d^\dagger_{L\downarrow} d^\dagger_{R\uparrow} |\Phi\rangle$ to form a spin singlet $|\tilde\Psi_1\rangle = P_G(d^\dagger_{L\uparrow} d^\dagger_{R\downarrow} - d^\dagger_{L\downarrow} d^\dagger_{R\uparrow})|\Phi\rangle$. However, the entanglement spectrum of $|\tilde\Psi_1\rangle$ would then correspond to two copies of spin-1/2 conformal towers due to the entanglement cut of an additional nonlocal singlet formed by a pair of two spin-1/2 semions at the boundaries [70].

This parton construction of MESs for the SU(2) CSL can be naturally generalized to the SU(N) CSL. To allow for exact zero modes, the hopping parameters in Eq. (3) are chosen as $t_x = t_y$ if N is even, and $t_x = t_y \cos(\pi/N)$ otherwise. This ensures that the exact zero modes, $d^\dagger_{L\sigma}$ and $d^\dagger_{R\sigma}$, appear at $k_y = \pi/N$ (see Fig. 7), which is always allowed for a suitably chosen boundary condition (i.e., periodic or twisted) in the y direction. Occupying N of these boundary modes distributed arbitrarily over left and right boundaries ensures that the total momentum of the state in y-direction is zero. As such this is then consistent with a width-N cylinder with plain periodic boundary conditions around the cylinder.

With that, MESs belonging to N different topological sectors can be written in analogy to the SU(2) case as

$$|\Psi_p\rangle = P_G \left(d^\dagger_{L1} \ldots d^\dagger_{Lp} d^\dagger_{R,p+1} \ldots d^\dagger_{RN} |\Phi\rangle \right) \qquad (4)$$

$p = 0, \ldots, N$. Here $d^\dagger_{L(R)\sigma}$ creates an elementary anyon of the chiral $SU(N)_1$ theory and also transforms under the SU(N) fundamental representation. Therefore $p = 0$ (N) corresponds to all N anyons either located, equivalently and respectively, at the left or right boundary. The entanglement spectra of these states $|\Psi_p\rangle$ should be in one-to-one correspondence with the N Kac-Moody conformal towers of the chiral $SU(N)_1$ WZW model, whose N primary fields are labeled by Young diagrams with p vertical boxes, respectively. However, except for $p = 0$ or N the states above do not yet describe proper SU(N) multiplets. For a more direct comparison with CFT, the N boundary modes need to be antisymmetrized over all flavors into an overall SU(N) singlet. The corresponding SU(N) singlets can be written as

$$|\tilde\Psi_p\rangle = P_G \left(\varepsilon_{\sigma_1 \ldots \sigma_N} d^\dagger_{L\sigma_1} \ldots d^\dagger_{L\sigma_p} d^\dagger_{R\sigma_{p+1}} \ldots d^\dagger_{R\sigma_N} |\Phi\rangle \right), (5)$$

where $\varepsilon_{\sigma_1 \ldots \sigma_N}$ is the totally antisymmetric Levi-Civita tensor. Eq. (5) indicates that for non-identity sectors, multiple branches contribute to the entanglement spectrum. The number of branches is $\frac{N!}{(N-p)!p!}$, where $N!$ comes from the Levi-Civita tensor, and the factors $(N-p)!$ and $p!$ account for the antisymmetrization of the anyons on the left or right

edge, represented by $N - p$ or p vertical boxes in the corresponding Young tableau, IRREPS $\bar{p}$ and p, respectively. Note that as such this precisely also corresponds to the dimensions $\dim(\text{aIR}_N(p)) = \dim(\text{aIR}_N(N - p))$ [see Sec. II C above].

Using the matrix-product-operator matrix-product-state (MPO–MPS) method of Ref. [67] to implement the parton construction, we can express the filled Fermi sea of the above parton wave function $|\tilde{\Psi}_p\rangle$ as an MPS. The principal idea for that is as follows: (i) the vacuum state $|0\rangle$ is an MPS with bond dimension $D = 1$. (ii) the non-local parton operator $d_{k\sigma}^\dagger$, subject to Wannier localization, can be written as an MPO of bond dimension $D = 2$. (iii) the MPOs $d_{k\sigma}^\dagger$ are applied sequentially onto the MPS with possible compression after each step, resulting in an MPS with a finite bond dimension that represents a filled Fermi sea. (iv) the Gutzwiller projector $P_G = \prod_{\ell=1}^L P_\ell$ is applied to separately enforce the local constraint, $\sum_\sigma c_{m,n,\sigma}^\dagger c_{m,n,\sigma} = 1$, on each site to recover the correct local physical subspace.

B. Infinite DMRG

For a cylinder geometry, the N different minimally entangled states of the SU(N) CSLs, each carrying distinct anyonic flux threading through the hole in the annulus, form a complete basis for the N-fold degenerate ground states. Finding such a complete basis numerically for the Hamiltonian of Eq. (1) would be a convincing validation for our short-range CSL proposal.

Numerically the finite system width N_y lifts the N-fold ground-state degeneracy, with an energy gap which decreases with increasing width. If the cylinder is infinitely long, CFT predicts that the energy splittings (with respect to the ground state) are given by $\frac{2\pi v}{N_y}(h_p + \bar{h}_p)$, where v is the velocity of the chiral edge states and $h_p, \bar{h}_p$ are conformal weights of the primary fields (corresponding to the respective anyons at the boundaries). Thus, we expect a power-law splitting $\mathcal{O}(1/N_y)$ for chiral topological phases (rather than exponential, as in the case of nonchiral topological phases with gapped edges [5, 71, 72]). This hampers the search for distinct topological sectors via DMRG, a ground-state search algorithm when using cylinders. Previous DMRG works [31, 72–77] have shed some light on this, showing that the presumably higher-energy states can still be examined by adopting tailored boundaries, e.g. imposing $\mathbb{Z}_N$ charges [78]. Concretely, DMRG is used to optimize the bulk part of the cylinder, while a small portion of spins at the boundaries are engineered to mitigate finite-width effects, thereby favoring different topological sectors if any exist. However, how to engineer the boundary spins and choose suitable lattice orientation remains an elusive undertaking.

Our work here is an extension of the above idea, and the parton approach paves a systematic way to construct the boundary spins for different MESs. For the identity sector, we use typical infinite DMRG (iDMRG) to find the ground state for Eq. (1) [79, 80]. For other sectors that are higher in energy, we use the parton approach outlined above to initialize

several possible MESs by occupying edge modes in different ways, then use the infinite DMRG algorithm to minimize the (bulk) ground-state energy with respect to the Hamiltonian of Eq. (1) for each. The ED calculations in Sec. II suggest a substantial region of a gapped CSL in the parameter space of $(\theta, \phi) = (\sin^{-1}(J_I), \tan^{-1}(\frac{3}{4}J_1/J_R))$ for each N. Here we focus on only one point within that phase, for $N = 2$ up to 4. While $N = 2$ and 3 have been investigated by ED and iPEPS previously, a thorough DMRG study for them has not been performed. We therefore include them here too, to corroborate the consistency of the model as well as the method for different N. We choose $(\theta, \phi) = (\pi/12, \pi/2)$ for $N = 2$, $(\theta, \phi) = (\pi/6, \pi/2)$ for $N = 3$, and $(\theta, \phi) = (\pi/4, \pi/2)$ for $N = 4$. The widths of the cylinder are chosen to be a multiple of N, so that if N different MESs do exist, all of them they can be found for arbitrary cylinder lengths.

The entanglement spectrum, as the fingerprint of topological order, can be readily extracted from iDMRG wave functions. To enable a comparison with CFT, we identify the entanglement levels by their SU(N) irreps and the momentum $k_y = \frac{2\pi K_y}{N_y}$, $K_y \in \mathbb{N}$ [72], as the converged states should be translationally invariant along the y direction. They are thus (approximate) eigenstates of the translation operator, with phase factors as eigenvalues, from which we extract the associated momenta k_y. From Fig. 8 (a), we see that the identity sector agrees with the SU(2)$_1$ WZW CFT (see Table IV) for the first few low-lying states. For the semion sector, the ES (see Fig. 8 (b)) consists of a new conformal tower containing integer spin multiplets, and twice the number of states expected for the semionic conformal tower. This discrepancy is rooted in the fact that semions carry spin-1/2 quantum numbers and can be best understood from the parton context [67]: the CFT content describes a single edge mode for spin-1/2, while the state in our simulation is a spin-singlet, corresponding to an antisymmetric combination of two spin-1/2 edge modes. In other words, neither of the semion states carrying spin-1/2 at the edges, i.e., $|\Psi_1\rangle = P_G d_{L\uparrow}^\dagger d_{R\downarrow}^\dagger |\Phi\rangle$ or $|\Psi_{1'}\rangle = P_G d_{R\uparrow}^\dagger d_{L\downarrow}^\dagger |\Phi\rangle$, does have a definite total spin. A spin-singlet can be formed, however, via a linear combination of $|\Psi_1\rangle$ and $|\Psi_{1'}\rangle$, which leads to the doubling of the number of states of the conformal towers [81]. This can be easily verified by a direct product of the conformal towers of the spin-1/2 primary of Table V (App. C) with a spin-1/2, as shown in Table II. This observation applies also for cases of $N > 2$: for non-identity sectors, the ESs contain, in each Virasoro level, an integer multiplicity ($\geq N$) of the number of states of a single CFT tower. In general, it is possible to account for such a multiplicity by taking the direct product of each conformal tower with the conjugate of its primary spin (see Tables XXVI , XXVII and XXVIII in App. F as examples). This brings our simulations in overall agreement with CFT as shown in Figs. 9 and 10 for $N = 3$ and $N = 4$, respectively, and a direct comparison with Tables XXVI, XXVII and XXVIII (see App. F). Conversely, one also could have 'quenched' the edge spins p and $\bar{p}$ in the DMRG simulation by coupling them to an artificial additional physical edge site with spin $\bar{p}$ and p at the left and right boundary, respectively. However, we refrained from
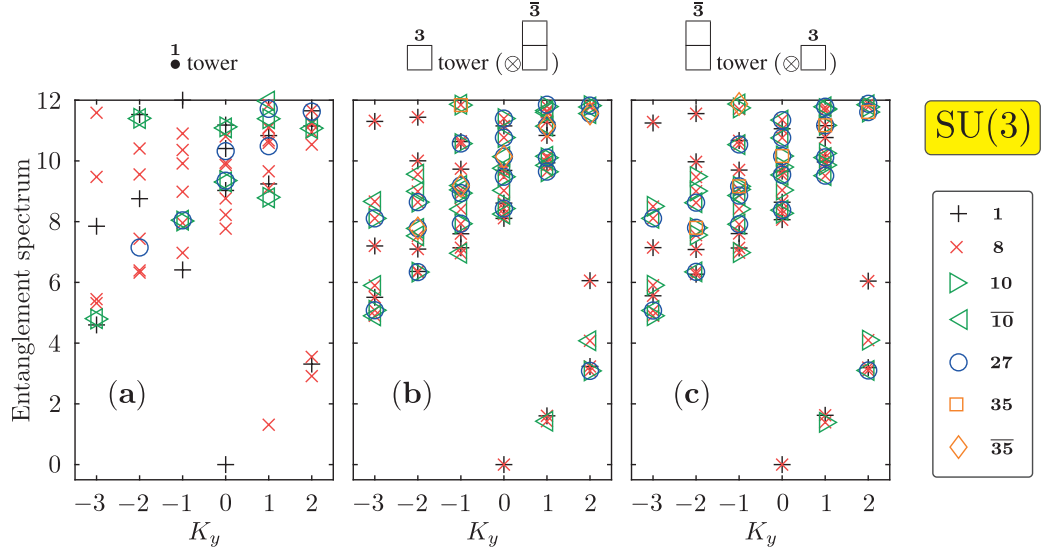
FIG. 9. The entanglement spectra on width-6 cylinders for SU(3) CSLs. **(a)** Identity sector. **(b)** ▢ sector (⊗▢). **(c)** ▢ sector (⊗▢). Identifying K_y with the Virasoro level L_0, the content of the chiral branches agrees exactly with the CFT predictions of tables VI and XXVI up to $K_y = 3$ (mod[6]). Note that the towers of the **3** and **3̄** sectors are identical, apart from an overall conjugation of all IRREPs.
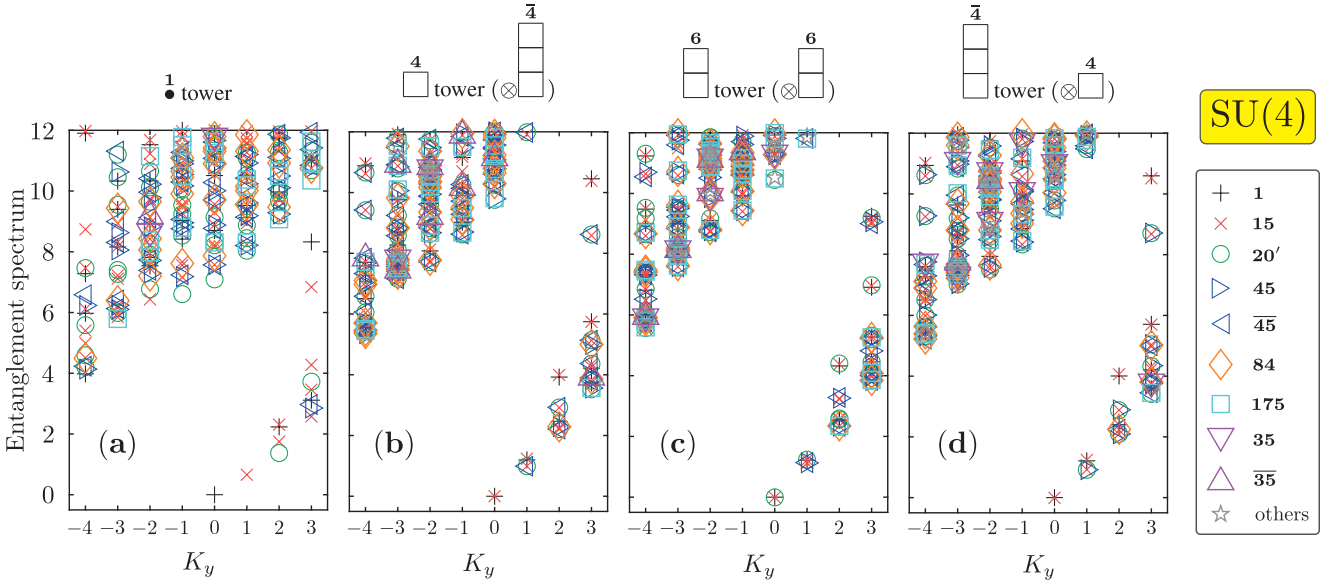
FIG. 10. The entanglement spectra on width-8 cylinders for SU(4) CSLs. **(a)** Identity sector. **(b)** ▢ sector (⊗▢). **(c)** ▢ sector (⊗▢). **(d)** ▢ sector (⊗▢). Note that the towers of the **4** and **4̄** sectors are identical, apart from an overall conjugation of all IRREPs. Identifying K_y with the Virasoro level L_0, the content of the chiral branches agrees exactly with the CFT predictions of tables VIII, XXVII and XXVIII up to $K_y = 3$.

	{0,0, 3,1}	{0,1, 0,3}	{1,0, 1,2}	{1,3, 0,0}	{3,0, 1,0}	{0,2, 1,1}	{2,1, 0,1}	{1,1, 2,0}
A_1		1	2	1	2	3	3	4
A_2	1		1	2	2	3	3	5
B_1		1	2	1	2	3	3	4
B_2	1		1	2	2	3	3	5

TABLE III. Number of symmetric site-tensors in each class characterized by the IRREP of the C_{4v} point group of the square lattice (rows) and the occupation numbers $\{n_{\mathbf{6}}, n_{\mathbf{4}}, n_{\bar{\mathbf{4}}}, n_{\mathbf{1}}\}$ of the $\mathbf{6}$,$\mathbf{4}$, $\bar{\mathbf{4}}$ and $\mathbf{1}$ multiplets on the 4 virtual bonds (columns).
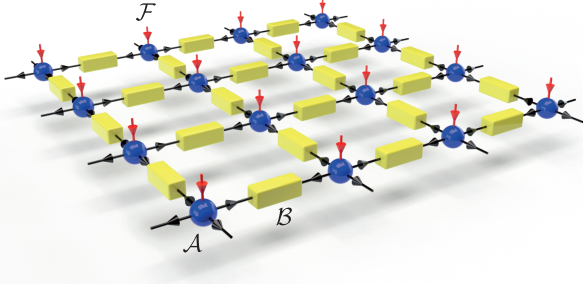
FIG. 11. PEPS on the square lattice involving site $\mathcal{A}$ tensors and bond $\mathcal{B}$ tensors. The bond dimension on the black links is D, up to $D^* = 4$ ($D = 15$), and the vertical red segments correspond to the physical space $\mathcal{F}$ spanned by the $d = N$ ($d^* = 1$) physical degrees of freedom. All indices (i.e. legs or lines) carry arrows which indicate whether legs enter or leave a tensor in terms of state space fusion. This can be translated into co- and contravariant tensor index notation, respectively [82, 83]. Note that reverting an arrow also flips all affected IRREPS into their dual representations.

doing so.

To summarize: in this section we have shown that a DMRG ground-state search for the Hamiltonian of Eq. (1), initialized with an MPS obtained via Gutzwiller-projected parton construction, yields entanglement spectra in excellent agreement with the expectations for $SU(N)_1$ CSLs. At a technical level, this required thefollowing innovations: (i) the Gutzwiller projected wave functions for $SU(N)_1$ CSLs, including the MES basis on the cylinder, are systematically constructed; (ii) the powerful tensor network library incorporating non-Abeliansymmetry efficiently converts the projected wave functions into MPSs with high fidelity; (iii) the iDMRG is initialized with the MES basis and preserves theSU(N) symmetry. The combination of these innovative techniques allows us to obtain all N degenerate ground states of theSU(N)$_1$CSL and characterize them from the entanglement spectrum.

IV. IPEPS

The results obtained from ED and iDMRG have shown affirmative evidences for $SU(N)_1$ CSL in a wide range of parameters with arbitrary N. On the other hand, a variational ansatz capturing properties of the CSL phase is also highly desired, especially in terms of symmetric PEPS. Following the implementation of chiral PEPS for $N = 2$ (see

Refs. [44, 48, 52]) and $N = 3$ (see Ref. [47]), we will first outline the general scheme of the construction, with focus on how the relevant symmetries are realized on the local tensors. We then proceed to a variational optimization of the very few parameters. Finally, we investigate the entanglement properties and bulk correlations of the optimized chiral PEPS, confronting the results with general considerations.

A. Symmetric PEPS construction

Let us first extend the construction of chiral PEPS used for $N = 2$ (see Refs. [44, 48, 52]) and $N = 3$ (see Ref. [47] for more details). The PEPS is obtained by contracting the network represented in Fig. 11, i.e., by summing all virtual indices on the links connecting rank-$(z+1)$ site and rank-2 bond tensors, z being the lattice coordination number, $z = 4$ for the square lattice. The physical space $\mathcal{F}$ on every lattice site is spanned by $d = N$ states transforming according to the fundamental IRREP of SU(N). The choice of the virtual space on the $z = 4$ bonds around each site can be made following heuristic rules valid for all N. In other words, we construct a SU(N)-symmetric PEPS from site/bond tensors with virtual (or bond state) space,

$$\mathcal{V}_N = \bullet \oplus \square \oplus \cdots \oplus \left.\begin{array}{c}\square\\\square\\\square\end{array}\right\} N - 1 \qquad (6)$$

where the direct sum contains all N IRREPs defined by single column Young diagrams of 0 up to $N - 1$ boxes, consistently with the $N = 2$ and $N = 3$ cases, $\mathcal{V}_2 = \mathbf{1} \oplus \mathbf{2}$ and $\mathcal{V}_3 = \mathbf{1} \oplus \mathbf{3} \oplus \bar{\mathbf{3}}$ [84]. For the $N = 4$ case we then assume $\mathcal{V}_4 = \mathbf{1} \oplus \mathbf{4} \oplus \mathbf{6} \oplus \bar{\mathbf{4}}$ (with bond dimension $D = 15$). By construction, the bond state (or virtual) space remains the same when the direction of arrow in Fig. 11 is reverted, as $\mathcal{V}$ maps into itself when all IRREPs are flipped into their dual. Note that the site tensor $\mathcal{A}$ can be seen as a linear map (or projection) $(\mathcal{V}_N)^{\otimes z} \to \mathcal{F}$ onto the physical state space, and the bond tensor $\mathcal{B}$ as fusing bond state spaces into a fully entangled pair singlet state, $(\mathcal{V}_N)^{\otimes 2} \to \bullet$. As such, the tensors $\mathcal{A}$ and $\mathcal{B}$ explicitly correspond to the 'P' and 'EP' part in the acronym PEPS, respectively. Up to normalization, the bond tensor $\mathcal{B}$ corresponds to an orthogonal matrix inserted into each bond within the tensor network [82, 83]. It is real and defined as a weighted sum of three elementary (reflection-symmetric) tensors representing the three allowed fusion channels $\bullet \otimes \bullet \to \bullet$, $\mathbf{6} \otimes \mathbf{6} \to \bullet$ and $\mathbf{4} \otimes \bar{\mathbf{4}} \to \bullet$. As such, it does not add any variational degrees of freedom.

As for $N = 2$ and 3, we classify the SU(4)-symmetric site-tensors according to (i) the number n_α of α-IRREPs appearing on their $z = 4$ virtual bonds, $n_{\mathrm{occ}} = \{n_{\mathbf{6}}, n_{\mathbf{4}}, n_{\bar{\mathbf{4}}}, n_{\mathbf{1}}\}$ ($\sum n_\alpha = z$) and (ii) the (1-dimensional) IRREP of the C_{4v} point group of the square lattice [85] (see Table III). Since the chiral spin liquid only breaks P (parity) and T (time-reversal)
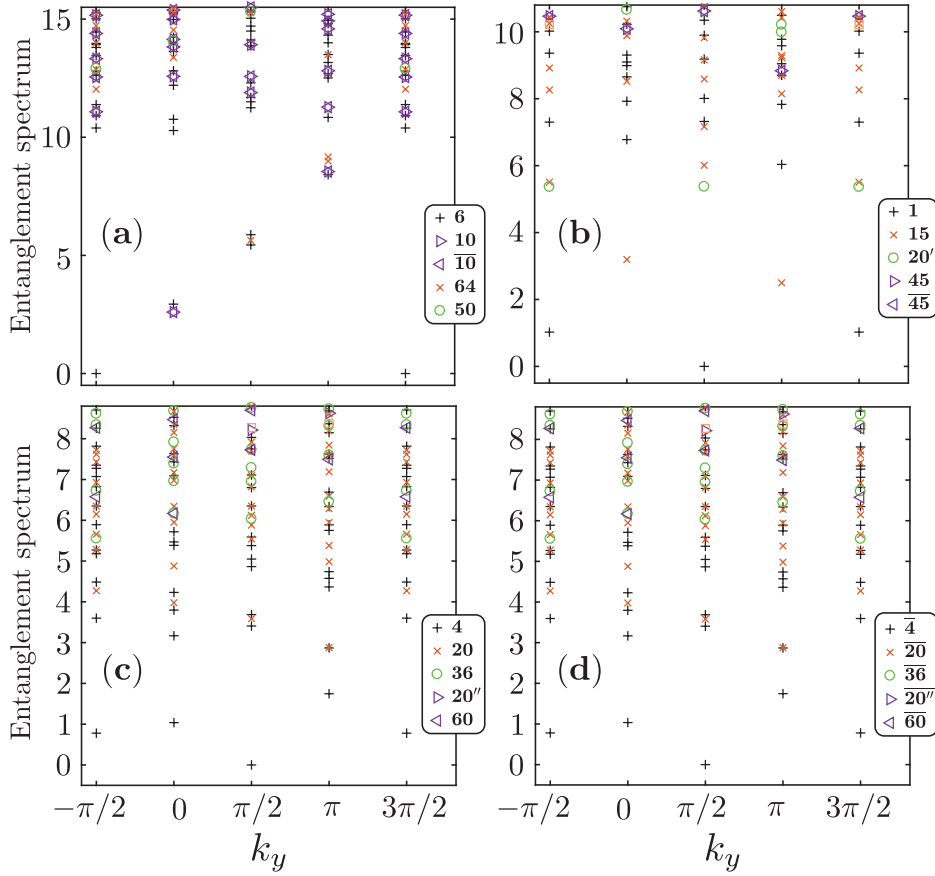
FIG. 12. Entanglement spectra on an infinitely-long width-4 cylinder obtained from an SU(4) ($D = 15$) PEPS wave function optimized for $\theta = \pi/4$, $\phi = \pi/2$ and environment dimension $\chi = 1350$. Spectra are plotted vs perimeter momentum k_y and, to better evidence their chiral nature, the $k_y = -\pi/2$ spectrum is replicated at $k_y = 3\pi/2$. Appropriate $\mathbb{Z}_4$ charge boundaries $Q = 2, 0$ and ± 1 are set up to select the **6 (a)**, **1 (b)**, and **4/$\overline{4}$ (c,d)** topological sectors, showing one, two and four branches, respectively. Note that the **4** and **$\overline{4}$** spectra are identical apart from an overall charge conjugation of all IRREPs (and small finite-χ numerical errors).

but does not break the product PT, the PEPS complex site tensor $\mathcal{A}$ should be invariant (up to a sign) under PT symmetry but acquires a complex conjugation under P or T separately (up to a sign). The simplest adequate ansatz has the following form:

$$\mathcal{A} = \mathcal{A}_R + i\mathcal{A}_I = \sum_{a=1}^{N_R} \lambda_a^R \mathcal{A}_R^a + i \sum_{b=1}^{N_I} \lambda_b^I \mathcal{A}_I^b, \quad (7)$$

where the real elementary tensors $\mathcal{A}_R^a$ and $\mathcal{A}_I^b$ either transform according to the A_1 and A_2 IRREPs, respectively, or according to the B_1 and B_2 IRREPs, respectively, giving rise to two possible families, $\mathcal{A}_A$ and $\mathcal{A}_B$. $N_R = 16$ and $N_I = 17$ are the numbers of the elementary tensors in each class and λ_a^R and λ_a^I are arbitrary real coefficients of these tensors to be optimized variationally.

To contract the infinite (double layer) tensor network, we have used the iPEPS method employing a Corner Transfer Matrix Renormalization Group (CTMRG) algorithm [86, 87] and obtain the fixed-point environment tensors used to compute the variational energy (on a 2×2 plaquette) or the entanglement spectra on infinite cylinders [47, 48]. In order to

cope with the large bond dimension ($D = 15$), the tensor contractions at each CTMRG step have been performed using the full SU(N)-symmetry, thanks to the QSpace library [82, 83]. This changes the description of any vector space $\mathcal{V}$ from state-based to multiplet-based. For numerical efficiency then, importantly, the dimensionality is reduced from $D_\mathcal{V}$ states to an effective dimension of $D_\mathcal{V}^*$ multiplets, where for SU(N) it typically holds $D_\mathcal{V}^* \ll D_\mathcal{V}$. As an example, the bond dimension $D^2 = 225$ of the double layer (rank-4) tensor $\mathcal{A}\mathcal{A}^*$ (used in CTMRG) can be reduced to $D^{2*} = 26$ which represents the number of multiplets in the product space:

$$\nu_4^{\otimes 2} = 4 \; \mathbf{1} \oplus 4 \; \mathbf{4} \oplus 4 \; \mathbf{4} \oplus 4 \; \mathbf{\overline{4}} \oplus 4 \; \mathbf{6} \oplus 1 \; \mathbf{10} \quad (8)$$
$$\oplus 1 \; \mathbf{\overline{10}} \oplus 3 \; \mathbf{15} \oplus 2 \; \mathbf{\overline{20}} \oplus 1 \; \mathbf{20'} \oplus 2 \; \mathbf{20}.$$

By fully enforcing SU(N) symmetries on all tensors and indices, this automatically implies that singular values within

any multiplet are degenerate. Therefore naturally, state space truncation is also always performed based on entire multiplets. Degeneracies across different multiplets, however, can be arbitrarily split depending on the algorithm and overall convergence. For SU(4), we have increased the environment dimension up to $\chi^* = 221$ multiplets (corresponding to $\chi = 1350$ states) to control truncation errors. The optimization of the PEPS (7) with respect to its variational parameters is done within a variational optimization scheme [88]. For $\theta = \pi/4$, $\phi = \pi/2$, the best variational energy (per site) $e \simeq -2.105$ (close to the DMRG estimate -2.14) is obtained for the $\mathcal{A}_B$ ansatz that we shall consider hereafter.

B. Entanglement spectrum and edge physics

Both ED and DMRG computations have shown overwhelming evidence of SU(N)$_1$ edge modes, both on disk and cylinder geometries, a fingerprint of the Abelian CSL phase. We note that, apart from the trivial (identity) sector, the conformal towers previously obtained using PEPS on cylinders for $N = 2, 3$ bear some differences with those obtained in DMRG. For example, the spin-1/2 semionic branch of the SU(2) spin-1/2 chiral PEPS corresponds exactly to the SU(2)$_1$ conformal tower – consisting of half-integer spin multiplets – associated to the WZW spin-1/2 primary field and its descendants, but with an exact two-fold degeneracy [44, 48, 52]. For the SU(3) spin-□ chiral PEPS, in the topological sectors defined by imposing $Q = \pm 1$ $\mathbb{Z}_3$ charges at the boundaries (stricly speaking, infinitely far away), three chiral branches – instead of a single one – separated in momentum by $2\pi/3$ are observed in the ES, whose level contents follow the prediction of the Virasoro levels of the SU(3)$_1$ WZW CFT [47]. Interestingly, both DMRG and PEPS show the same number of states in each Virasoro level, namely N times the WZW CFT content. These particular features of the PEPS ansatz are now further tested in the case of the SU(4) model in order to draw more general (empirical) statements for SU(N) spin-□ chiral PEPS.

The ES, revealing the topological properties of the PEPS, is computed by placing the optimized $D = 15$ ($D^* = 4$) PEPS on a width-4 infinite cylinder partitioned in two halves. The PEPS holographic bulk-edge correspondence [47, 89] enables to compute the ES simply from the (fixed-point) environment tensors. The four topological sectors are selected by imposing a well-defined total $\mathbb{Z}_4$ charge Q at both ends (strictly speaking at infinity) on the virtual levels. Following the assignment $q_1 = 0$, $q_4 = 1$, $q_{\bar{4}} = -1$ and $q_6 = 2$, we have $Q = \sum q_\alpha \bmod[4]$, where the sum runs over the virtual open bonds along the circumference at the boundaries. In practice, this is performed by filtering out the components of the environment tensors used to approximate each halves of the cylinder.

A necessary ingredient for identifying the linear dispersing modes in ES is the momentum quantum number associated with each energy level, which originates from the translation invariance along the circumference of the cylinder. For that purpose, we consider the momentum projection operator P_{k_y}:

$$P_{k_y} = \frac{1}{N_y} \sum_{r=0}^{N_y-1} e^{-ik_y r} T^r, \qquad (9)$$

where $k_y = \frac{2\pi}{N_y} K_y$, $K_y = 0, 1, 2, \ldots, N_y - 1$, and T is the one-site translation operator acting on the virtual degrees of freedom. Since T commutes with ρ, we can diagonalize $P_{k_y} \rho P_{k_y}$, whose nonzero eigenvalues are also eigenvalues of ρ, and corresponding eigenstates carry momentum quantum number k_y, to obtain ES and momentum quantum number simultaneously. In this setup, the action of translation operator on ρ can be implemented as a permutation of indices of ρ.

In Fig. 12 the ES in the four topological sectors are shown as a function of the momentum k_y along the circumference. For $Q = 2$, 0 and ± 1, we identify one, two or four linearly dispersing chiral branches, respectively. When two or four branches are seen, the later are equally spaced in momentum, i.e. by $2\pi/2 = \pi$ and by $2\pi/4 = \pi/2$, respectively. Despite the very small circumference ($N_v = 4$), for $Q = 2$ and 0 the expected SU(4)$_1$ counting of the first Virasoro levels is satisfied. For $Q = \pm 1$, due to limited resolution in K-space, the states of the second Virasoro level of each branch are not clearly separated from the continuum above. Although it is difficult to draw definite conclusions on such a thin cylinder, it seems that the SU(4) chiral PEPS reveals, as for the SU(2) and SU(3) cases, a duplication of the chiral branches for most topological sectors. In the SU(2) PEPS this was attributed to the so-called "dressed mirror symmetry" within the virtual degrees of freedom [90]. Note however that there is no exact degeneracy in the $N = 3$ and $N = 4$ cases, in contrast to $N = 2$, so that the duplication of the chiral modes may have a different origin here. In any case, as for the DMRG wave function, the duplication of the chiral states in the PEPS is linked to the fact that the ansatz is not a MES but, rather, carry an extra entanglement due to its global singlet nature. However, the manifestation in the ES is different in the two cases.

C. Correlation lengths

It was proven that any short-range quadratic parent Hamiltonian for chiral *non-interacting* PEPS is gapless [91]. This suggests that a fundamental obstruction or "no-go theorem" may prevent to describe a gapped CSL phase with a 2D PEPS (of finite bond dimension D). In fact, the PEPS optimized for the $N = 2$ and $N = 3$ chiral Heisenberg models [47, 48] reveal rather long-range correlations and growing correlation lengths with environment dimension χ. It is therefore of much interest to also test this important feature in our SU(4) PEPS. For that purpose, we have computed the leading correlation lengths (associated to the leading correlations in the bulk of the PEPS) from the leading eigenvalues of the transfer matrix (TM) [44] (with no gauge "vison" flux). These correlation lengths, plotted in Fig. 13, show no sign of saturation with χ^*/D^{2*}, or equivalently with χ/D^2 ($D = 15$) – at least the three largest ones. The latter (shown in orange color)
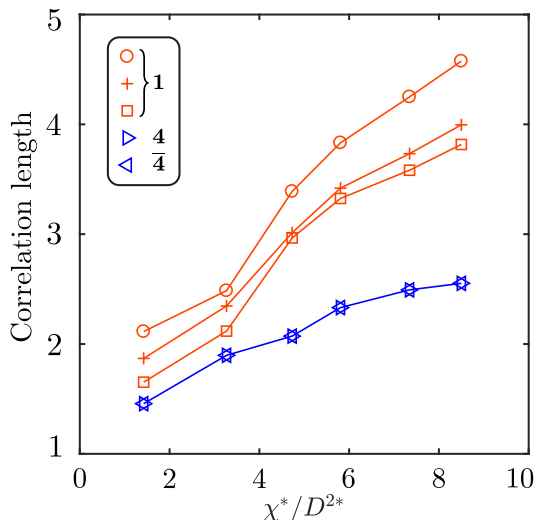
FIG. 13. Leading correlation lengths obtained from the transfer matrix (in the absence of gauge flux) for the case of SU(4) plotted versus the number of multiplets χ^* kept in the environmental tensors, normalized by $D^{2*} = 26$ which represents the number of multiplets in the product space of $D \times D$ states with D fixed. The SU(4) IRREPs associated to these correlation lengths are indicated.

have been obtained from the singlet eigenvalues of the TM and, probably, correspond to dimer correlations. The next two (shown in blue color) correspond to spinon correlations. We note that all correlation lengths remain rather short, even for the largest χ value. However, the data for $N = 2$, 3 and 4 clearly show that all correlation lengths are comparable at the same value of χ/D^2. For example, the dimer correlation length ranges between 3.5 and 6 for $\chi/D^2 = 6$, weakly dependent on N and on the model parameters. Since the PEPS bond dimension increases significantly with N ($D = 3, 7, 15$ for $N = 2, 3, 4$, respectively) the maximum achievable value of χ/D^2, and hence of the correlation lengths, decreases strongly with N.

Note that in the SU(2) case, the diverging nature of the correlation lengths was shown to be associated, not to a conventional critical behavior but, rather, to the existence of "long-range tails" (of very small weight) in most correlation functions [48]. We believe such a property also holds for any SU(N) CSL, although it could not be established here for $N = 4$ due to the large value of the bond dimension D.

V. CONCLUSION AND OUTLOOK

In this work, the previous family of SU(3) chiral Heisenberg models on the square lattice has been generalized to any SU(N) fundamental IRREP as physical degrees of freedom. The construction follows two steps: the first one consists in building up the most general fully translational, rotational and SU(N)-symmetric model (possibly breaking time-reversal symmetry) whose interactions extend at most to 3-sites within the square plaquettes. In a second step, one restricts to a subset of this model family whose Hamiltonians

can be written solely as a sum of S_3-symmetric operators defined on all the triangles within the square plaquettes. By doing so, we expect to mimic some of the physics of the triangular lattice with 3-site chiral interactions, although keeping the full C_{4v} point group symmetry of the square lattice. This procedure defines a sub-family of chiral Heisenberg models spanned by two independent parameters (angles) that we have explored in details.

Extensive ED computations bring overwhelming evidence of extended regions of stability of SU(N) CSL phases for all N, up to $N = 10$. The Abelian SU(N)$_1$ topological nature of these phases has been clearly established from the many-body low-energy spectra of periodic (tori) and open (disks) clusters. When the system size N_s is commensurate with N (so that no anyons is present in the GS) a N-fold GS degeneracy is observed on small tori as expected. When the commensurability between N_s and N is such that a single quasi-hole populates the GS, N_s quasi-degenerate GS are found, as expected. Finally, chiral many-body low-energy spectra on open clusters following WZW CFT counting rules provide an even more stringent test of the existence of the SU(N)$_1$ Abelian CSL.

iDMRG computations by enabling to access much larger systems – typically infinitely-long broad cylinders – provide most valuable and complementary results for $N = 2, 3, 4$. Gutwiller-projected parton wave functions offer a guide to construct iDMRG ansatze in each topological sector. Due to their SU(N) global singlet nature, the iDMRG wave functions carry larger entanglement than MES (they can be seen as linear combinations of MES, except in the trivial sector) and, hence, show ES with more structure whose complete understanding has been fully provided.

Following the prescriptions for $N = 2$ and $N = 3$, we have constructed a family of chiral SU(4)-symmetric PEPS and, under optimization, a good variational PEPS ansatz is obtained for the chiral SU(4) Heisenberg model. The entanglement spectra obtained in the $N = 4$ topological sectors of an infinitely-long cylinder reveal chiral modes. The multiplicity of the chiral modes is attributed to the non-MES nature of the singlet PEPS ansatz in most topological sectors. Finally, growing correlation lengths with environment dimension are consistent with the existence of "long-range tails" (of very small weight) in correlation functions (evidenced explicitly for $N = 2$ [48]). We speculate that these long-range tails would fade away (i.e. their weights would continuously vanish) for increasing D, providing a more and more faithful representation of the GS. If correct, this implies that the no-go theorem [91] does not *practically* prevent an accurate chiral PEPS representation of the topological gapped CSL phase.

We note that the SU(N) CSL is stable in some regime where the 3-site interaction is purely imaginary (corresponding to $\phi = \pi/2$, mostly studied here. In fact, this case is relevant in ultracold atom systems which can realize an SU(N) fermionic Hubbard model [27]. In the presence of an artificial gauge field (providing complex amplitudes to the effective hoppings), at $1/N$ filling (one particle per site), the large-U Mott insulating phase [19, 29, 30] can be approximately described by our Hamiltonian, so that an Abelian SU(N) phase on the square lattice may be seen experimen-

tally if low-enough temperatures could be reached. Experimental setups of ultracold atoms at other fractional fillings like k/N ($k \in \mathbb{N}$ particles/per site) could be also of great interest and be described by new types of SU(N) spin Hamiltonians, like the two-fermion SU(4) model [92] with additional chiral interactions on triangular units, opening the way to observe non-Abelian CSL.

Appendix A: Analysis of 2×2 plaquette

The focus of the present paper is on chiral spin liquids which have the SU(N) flavor symmetry intact both locally and globally. In particular, the ground state remains an SU(N) singlet in the thermodynamic limit. This suggests that also the low-energy regime of smaller clusters should have a singlet ground state. If that is not possible by finite size, at least, one may expect to have a ground state that is closest to a singlet in the sense that they tend to prefer to fill up full columns in the corresponding Young tableau (YT).

In this spirit this appendix analyzes the 2×2 plaquette as an elementary unit of the Hamiltonian. The Hamiltonian (1) on the full 2D square lattice can be rewritten as

$$H = \sum_p H_p \tag{A1}$$

where H_p is the Hamiltonian for a single square plaquette p of 2×2 sites that combines all terms $i, j, k \in p$ (in order to avoid overcounting along the edge of the plaquette, we set $J_1 \to \frac{1}{2}J_1$ for H_p, whereas J_2, J_R, and J_I remain the same). Now with H_p the combined set of local operators that can be used to tile the entire 2D Hamiltonian, it is natural to analyse its multiplet structure. Multiplets in H_p that are low in energy are expected to be important in the low energy physics on the 2D lattice itself, whereas multiplets of H_p at higher energies will likely play a minor role. Clearly, the ground state multiplet of H_p also may change when tuning the coupling parameters $\{J_1, J_2, J_R, J_I\}$. This then may signal a qualitative change of the overall low-energy behavior of the 2D system, e.g., a low-order phase transition for similar coupling parameters.

The eigenspectrum of the 2×2 plaquette Hamiltonian H_p is analyzed in Fig. 14 for $N = 2, 3, 4, 5$ in panels (a-d), respectively. The SU(N) multiplet structure is fully resolved as indicated with the legend. For the sake of the discussion here, we use Dynkin labels in compact notation to identify symmetry sectors where $q \equiv (q_1 \ldots q_{N-1})$ directly specifies to corresponding SU(N) YT via differential length offsets of the number of boxes in subsequent rows of the YT (e.g. see also App. A in [93]). For example, $(10 \ldots 0)_{N-1}$ is the fundamental or defining representation also labelled as **N** in the main text, and $(10 \ldots 01)_{N-1}$ is the adjoint representation. The reverse order $(q_{N-1} \ldots q_1) \equiv \bar{q}$ specifies the dual IRREP to any $q = (q_1 \ldots q_{N-1})$. For the case of SU(2), having a single number (q_1) only, the integer q_1 simply counts the total number of boxes in the YT, and thus corresponds to a spin $S \equiv q_1/2$ multiplet. Its adjoint is given by $S = 1$, i.e. multiplet $q = (2)$.

General aspects of SU(N) permutation Hamiltonian

The Hamiltonian (1) and therefore also H_p above is defined via simple permutations of flavors over two or three sites. A direct consequence of this is, that all eigenenergies appearing for SU(N) exactly also must appear for SU($N' > N$), as can be clearly observed in Fig. 14. The simple reason is that adding additional flavors $N' - N > 0$ on top of all
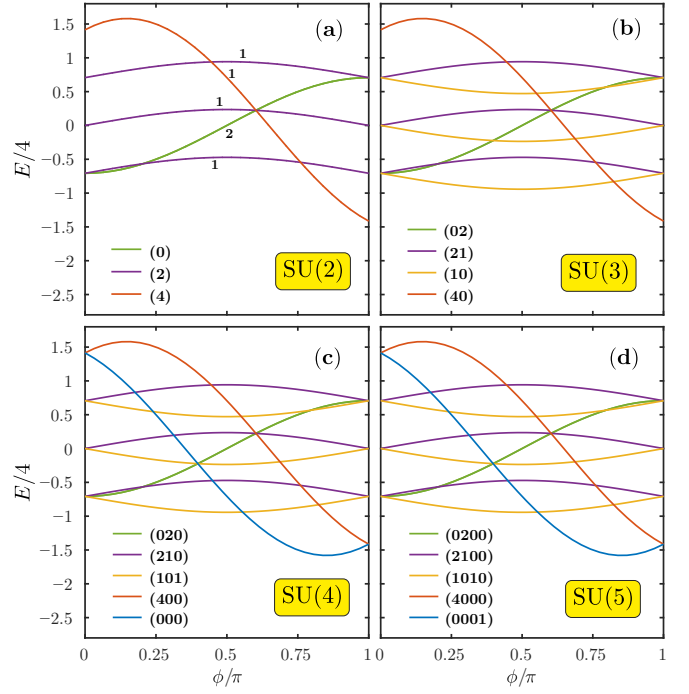
FIG. 14. Eigenspectrum of a 2×2 cluster described by the plaquette Hamiltonian H_p in Eq. (A1) vs. ϕ using the parametrization in Eq. (2), with $\theta = \pi/4$ fixed as in the main text [e.g. see Fig. 2]. To focus on energy per site, the energies are divided by the number of sites $N_s = 4$ as indicated. Panels (a-d) refer to case of $N = 2, 3, 4, 5$ symmetric flavors, respectively. Colors indicate symmetry sectors as indicated with the legend based on Dynkin labels. The small numbers on top of each line in panel (a) indicate the degeneracy of multiplets which shows that the green line only is 2-fold degenerate. This also holds for all data in the other panels.

sites, the Hamiltonian will not make any reference to these when applying it to a state that only contains up to the first N flavors. The multiplet label needs to adapt, though. By using Dynkin labels, this simply concatenates additional trailing numbers q_i. Considering a four-site plaquette here, these extra trailing numbers must all be zero for $N' > 4$, as largely already also observed for SU(4) itself [see legend in Fig. 14(d)]. With this clearly also the degeneracy in terms of states within these multiplets changes as required by the increased Hilbert space. However the eigenenergies themselves remain exactly the same. Therefore given a Hamiltonian that solely consists of permutations of otherwise symmetric flavors, the many-body eigenspectrum for a given SU(N) is exactly inherited also to all cases SU($N' > N$). This is made explicit across the panels in Fig. 14 by choosing matching color coding. For example, what was a singlet in SU(2), i.e., the green line for $q = (0)$, becomes $q = (02)$ for SU(3), and then $q = (020 \ldots)$ for larger N still.

When increasing the number of flavors $N \to N' > N$, however, also new eigenenergies can emerge that were previously absent. For example, in Fig. 14 this is seen as additional lines that appear when going from $N = 2 \to 3$ (yellow lines) or $N = 3 \to 4$ (blue line). Given a 4-site plaquette with the

fundamental IRREP on each site, the number of lines will no longer change for $N' > 4$, as seen by going from $N = 4 \to 5$, since all YTs with four boxes are already present.

Low-energy regimes

Now the analysis in Fig. 14 tracks the eigenvalues vs. ϕ for fixed $\theta = \pi/4$ similar to Fig. 2 in the main text. The red line in Fig. 14 corresponds to the fully symmetric IRREP $q = (40\ldots)_{N-1}$ that is present for all $N \geq 2$. This multiplet crosses over and becomes the ground state for $\phi > \pi$ for $N \geq 4$, and already earlier for $N = 2$ and $N = 3$. This shows that the 2×2 plaquette becomes ferromagnetic around $\phi \gtrsim \pi$ [note that based on Eq. (2), $\phi > \pi$ corresponds to negative, and hence ferromagnetic J_1 and J_2]. As such, this signals the onset of ferrogmagnetism on the full 2D system, also consistent with the analysis of the larger clusters in Fig. 2.

Finally, with focus on a singlet ground state, on the given four-site plaquette this can only be achieved exactly for $N = 2$ and $N = 4$. Interestingly then, the singlet for SU(2) [green line in Fig. 14(a)] becomes a non-singlet for $N > 2$, i.e., (02) for SU(3), and $(020\ldots)$ thereafter. Instead, an entirely new singlet shows up for SU(4) in the low-energy regime, and remains an eigenenergy for $N \geq 4$ (blue line). Therefore while in the case of SU(2) the singlet is favored for small $\phi \in [0, \pi]$, it is favored for larger $\phi \in [0, \pi]$ for SU(4) and onward. What comes closest to a singlet for SU(3) on the 2×2 plaquette, on the other hand, is the multiplet (10), i.e. the fundamental IRREP. Based on the fusion of the four fundamental IRREPs on the 2×2 plaquette to start with, this already fused three of these into a singlet. As seen by the yellow line in Fig. 14(b), the multiplet (10) is the ground state for a wide range $\phi \in [0, \pi]$, including small but excluding large ϕ where the system becomes ferromagnetic. This is perfectly consistent with the analysis on the larger cluster in Fig. 2(a) in the main text which for $N = 3$ also shows the chiral phase extending all the way down to $\phi = 0$.

The chiral phase was identified in Fig. 2 with the gapped phase around $\phi \gtrsim \pi/2$. However, when reducing ϕ, as seen in Fig. 2 for $N > 3$, this gapped phase closes at finite ϕ. Even more, for certain N it appears to reopen before approaching $\phi = 0$. Hence based on Fig. 2 having the chiral phase identified with the regime of larger $\phi \gtrsim \pi/2$, this is entirely consistent with the regime in the present analysis of the 2×2 plaquette where the system is (or tends towards becoming) a singlet for $N \geq 4$ in Fig. 14(c,d). Note that for $N > 4$, the blue line in Fig. 14(d) corresponds to the fully antisymmetric multiplet where four boxes are stacked on top of each other into a single column in the corresponding YT.

In the chiral regime $\phi \gtrsim \pi/2$ also the coupling strength of the real three-site permutation term $H_{ijk}^R \equiv J_R(P_{ijk} + P_{ijk}^{-1})$ turns negative, i.e., having $J_R < 0$. Its effect is revealed by looking at the eigenvalues in the 3-site eigenbasis for given triangle triangle (ijk). One finds for $N \geq 3$ that the completely symmetric multiplet $(30\ldots)$ and the completely antisymmetric multiplet $(001\ldots)$ [equivalent to (00) for SU(3)] are eigenstates to the same eigenvalue $+2J_R$, whereas the

2-fold degenerate multiplets $(110\ldots)$ have eigenvalue $-J_R$ (which are eventually differentiated by the complex term J_I). Hence negative J_R equally favors both, the completely symmetric multiplet (ferromagnetic) as well as the completely antisymmetric multiplet (antiferromagnetic) on any triangle. When considering all triangles within a 2×2 plaquette as analyzed in Fig. 14, the antiferromagnetic states dominate the low energy regime, yet with the ferromagnetic regime in close proximity (both , the blue and red lines move downward with increasing ϕ for $N \geq 4$). Eventually, for $\phi > \pi$ when also the two-site exchange couplings J_1 and J_2 turn negative, the ferromagnetic state takes over.

Appendix B: Generalized exclusion principle for Abelian SU(N) CSL

We provide here complementary details about the heuristics on the content (degeneracy, quantum numbers, etc...) of the GS manifold within the CSL phase on small periodic clusters (of torus geometry).

As realized already for $N = 3$ in Ref. [47], it is possible to obtain, for arbitrary N, the exact momenta of the various states in the GS manifold expected for an Abelian SU(N)$_1$ CSL. This can be inferred from a simple generalized exclusion principle (GEP) known for FQH states [59] or fractional Chern insulators [60] with clustering properties.

For our SU(N) model in the fundamental representation, there are N states per site which can be viewed as a color degree of freedom. The mapping to a bosonic FQH requires to treat them separately: one (arbitrarily chosen) color will correspond to a hole while the remaining $C = N - 1$ will correspond to spinful SU(C) bosons. Hence, Abelian bosonic FQH states can be constructed at a filling $\nu_{FQH} = C/(C + 1) = (N - 1)/N$, corresponding to Halperin states [94–96]. In this terminology, the ground states and quasi-hole states is given by the number of dressed partitions $(1, 2)_C$, see Ref. [60]. Moreover, the respective momenta can be obtained from the mapping between N_s orbitals obtained when folding the Brillouin zone [97, 98].

To be more specific, let us consider for instance $N = 3$ which maps onto $C = 2$ bosons, i.e spin-1/2 particles. Then, the generalized exclusion principle for the ground-states (for $N_s = kN$) enforces the occupations $(\downarrow, \uparrow, 0, \ldots)$ and its translations, i.e. 3 states. This $(1, 2)_2$ exclusion rule simply enforces that identical particles cannot be neighbors but a $\downarrow$ particle can be followed by a $\uparrow$ particle. Such rules can be rephrased in terms of follow-up rules in the string of states, e.g. $0 \to (0, \downarrow, \uparrow)$, $\uparrow \to 0$, $\downarrow \to (0, \uparrow)$, which defines a "transfer matrix",

$$T^{(N=3)} = \begin{bmatrix} 1 & 1 & 1 \\ 1 & 0 & 1 \\ 1 & 0 & 0 \end{bmatrix}, \tag{B1}$$

for $N = 3$.

The transfer matrix above is easy to generalize to any N, with 1's in the first column and above the diagonal and zeros

otherwise. For example, one gets

$$T^{(N=5)} = \begin{bmatrix} 1 & 1 & 1 & 1 & 1 \\ 1 & 0 & 1 & 1 & 1 \\ 1 & 0 & 0 & 1 & 1 \\ 1 & 0 & 0 & 0 & 1 \\ 1 & 0 & 0 & 0 & 0 \end{bmatrix}, \qquad (B2)$$

for $N = 5$. Note that, in addition to the rules encoded in the transfer matrix (which alone produce a large number of irrelevant configurations), one should also simultaneously enforce a global property relating the total appearance of all colors such that the GS belong to the SU(N) IRREP of smallest possible dimension compatible with system size. More precisely, defining the integer $r_0 = \mathrm{mod}(N_s, N)$, the smallest possible IRREP corresponds to the antisymmetric IRREP with a Young diagram of r_0 vertical boxes (labeled in the text aIR$_N(r_0)$), and, heuristically, is to be associated to the GS manifold. For instance for $N_s = kN$, all colors should appear exactly k times, i.e. $c_1 = c_2 = \cdots = c_N = k$, as the singlet character of the GS manifold implies.

For $N_s = kN - 1$, $k \in \mathbb{N}$, we expect the low-energy states to represent the quasi-hole excitations, similar to the quasi-hole Laughlin states when inserting a flux in a fractional quantum Hall state on a torus. In particular, the quasi-hole counting on a finite cluster should be the same as in the thermodynamic limit and is given by a generalized Haldane exclusion principle [97, 98]. Moreover, the lattice momenta at which these (quasi) degenerate states sit can be obtained using a heuristic rule by folding the two-dimensional Brillouin zone into a one-dimensional lattice of orbitals [97]. For instance, for all the quasi-hole examples shown in Fig. 4, since GCD(N, N_s)=1, we expect to find one low-energy SU(N) multiplet at each momentum (i.e. a total number of quasi-hole states equal to NN_s), which is exactly what is found numerically.

When $N_s = kN$, we expect N-fold quasi-degenerate ground states on a torus. The momenta are given using a similar heuristic rule and are non-trivial. For completeness, here are the predictions corresponding to the values shown in Fig. 4 (see the Brillouin zones as insets for the momenta notations): (i) $N = 4$ and $N_s = 20$: one state at momentum Γ, M and 2-fold degenerate X; (ii) $N = 5$ and $N_s = 15$: one state at momentum Γ, $\pm\Sigma_0$, $\pm\Sigma_2$; (iii) $N = 6$ and $N_s = 12$: one state at momentum Γ, Z_1, $\pm\Delta$, Z_0, Δ; (iv) $N = 7$ and $N_s = 14$: one state at momentum Γ, ± 0, ± 2, ± 5. All these predictions are verified numerically, and the low-energy states are always well separated from the higher excited ones as expected in this topological incompressible gapped phase.

Appendix C: WZW SU(N)$_1$ chiral towers of states

We provide here an almost self-contained explanation of the Hilbert-space structure of the SU(N) WZW CFT and derive the SU(N)$_1$ WZW towers of states for $N = 2$ to 8, which are to be compared with the ED results for SU(N) open clusters investigated and discussed in the main text. This appendix is organized as follow. In the first part, we recall some basic facts on $\mathfrak{su}(N)$ Lie algebra and its representation theory

(see Ref. [99] for a readable introduction to Lie algebras and their representation). In a second part, we briefly present the affine extension of SU(N) and introduce the primary states on which the Hilbert space is constructed. Most of the equations presented in the first two parts are relevant to any (affine) Lie algebras unless otherwise stated. In the last part, we explain how WZW SU(N)$_1$ chiral towers of states for open clusters can be computed using this formalism. The appendix closes with the tables showing the explicit form of the towers of states relevant for the present study, up to SU(8). This appendix in not intended to give a mathematical presentation of the field but rather to introduce, without any mathematical proof, the basic tools needed to identify the expected representations in WZW SU(N)$_1$ chiral towers of states.

1. $\mathfrak{su}(N)$ Lie Algebra

Group, Generators - The special unitary group SU(N) is the Lie group of $N \times N$ unitary matrices with determinant 1. The Lie algebra $\mathfrak{su}(N)$ associated to the Lie group SU(N) is determined by a set of $N^2 - 1$ traceless hermitian generators J^α satisfying the commutation relations,

$$\left[J^\alpha, J^\beta \right] = i f_{\alpha\beta\gamma} J^\gamma, \qquad (C1)$$

where the real fully antisymmetric tensor f encodes the structure constants. Equation (C1) is a direct consequence of the group structure of SU(N) and the fact that the Lie group and the Lie algebra are related by the exponential map which associate to any element J of $\mathfrak{su}(N)$ an element $\exp(itJ)$ of SU(N).

Cartan Weyl basis, Adjoint representation, roots - The maximal subset $\{H^i\}_{i=1,\dots,r}$ of $\mathfrak{su}(N)$ composed of commuting generators $[H^i, H^j] = 0$ forms the Cartan subalgebra of $\mathfrak{su}(N)$ and plays the role of S^z in $\mathfrak{su}(2)$. Obviously, since all H^i can be diagonalized simultaneously, the rank r of $\mathfrak{su}(N)$ is $N - 1$, which is equal to the maximal number of traceless diagonal $N \times N$ matrices. As $\{H^i\}$ can be simultaneously diagonalized, we can choose the basis vectors in any irreducible representation to be the eigenstates $|\boldsymbol{\mu}\rangle$ of H^i:

$$H^i |\boldsymbol{\mu}\rangle = \mu_i |\boldsymbol{\mu}\rangle . \qquad (C2)$$

The $(N-1)$-dimensional vector $\boldsymbol{\mu} = (\mu_1, \dots, \mu_{N-1})$ is called the weight. The remaining $N(N-1)$ off-diagonal generators will be denoted as $E^{\boldsymbol{\alpha}}$.

To each generator J^α, we can associate a linear map ad_J from $\mathfrak{su}(N)$ to itself defined as $\mathrm{ad}_J(X) = [J, X]$ for any X in $\mathfrak{su}(N)$. This defines the adjoint representation which can be used to classify the generators $E^{\boldsymbol{\alpha}}$ as eigenvectors of ad_{H^i} :

$$\mathrm{ad}_{H^i}(E^{\boldsymbol{\alpha}}) = [H^i, E^{\boldsymbol{\alpha}}] = \alpha_i E^{\boldsymbol{\alpha}} \quad (i = 1, \dots, N-1) . \qquad (C3)$$

The $(N-1)$-dimensional vectors $\boldsymbol{\alpha} = (\alpha_1, \dots, \alpha_{N-1})$ are called the roots and $E^{\boldsymbol{\alpha}}$, which play the role of $S^{\pm}$, the ladder operators. The Cartan-Weyl basis is $\{H^i, E^{\boldsymbol{\alpha}}\}_{i \in \{1,\dots,r\}, \boldsymbol{\alpha} \in \Delta}$ where Δ denotes the set of all $N(N-1)$ roots. Obviously, only $r = N - 1$ roots are linearly independent. An important

remark is the non-degeneracy of roots. Indeed, the existence of a degenerate root would contradict the definition of the Cartan subalgebra (<u>maximal</u> set of commuting generators).

It is clear from Eq. (C3) that there is some arbitrariness in the determination of $E^{\boldsymbol{\alpha}}$ and $\boldsymbol{\alpha}$ as both depend on the choice of a particular basis for the Cartan subalgebra. Nevertheless, some general properties can be established. Once the basis of $r = N-1$ linearly independent roots is fixed, one can expand any root in this basis. Roots with positive coefficients in this expansion are called <u>positive</u> and form the set Δ_+. A root $\boldsymbol{\alpha}^{(i)}$ $(i=1,\ldots,r)$ that cannot be expressed as an integer sum of two positive roots is by definition a <u>simple root</u>.

The central role of such $r = N-1$ simple roots not only lies in the fact they provide a convenient basis for roots but also because the $(N-1)\times(N-1)$ matrix A of the scalar products of simple roots (the <u>Cartan matrix</u>) completely encode the Lie algebra:

$$A^{ij} = \frac{2\boldsymbol{\alpha}^{(i)}.\boldsymbol{\alpha}^{(j)}}{\boldsymbol{\alpha}^{(j)}.\boldsymbol{\alpha}^{(j)}} = \boldsymbol{\alpha}^{(i)}.\boldsymbol{\alpha}^{(j)\vee}, \qquad (C4)$$

with $\boldsymbol{\alpha}^{(i)\vee} = 2\boldsymbol{\alpha}^{(i)}/|\boldsymbol{\alpha}^{(i)}|^2$ (<u>coroots</u>). The entries of this matrix are always integers and, in the $\mathfrak{su}(N)$ case, A is symmetric and take the form $A^{ij} = 2\delta_{ij} - \delta_{|i-j|,1}$. For $\mathfrak{su}(N)$ in which all the $N(N-1)$ roots have equal length (i.e., <u>simply laced</u>), it is convenient to choose $|\boldsymbol{\alpha}^{(i)}| = \sqrt{2}$ so that we do not need to distinguish between the roots and the coroots. The lattice spanned by the $r = N-1$ basis vectors $\boldsymbol{\alpha}^{(i)}$ ($\boldsymbol{\alpha}^{(i)\vee}$) is called the <u>root lattice</u> $\Lambda_{\mathrm{r}}(\mathfrak{su}(N))$ [the <u>coroot lattice</u> $\Lambda_{\mathrm{r}}^{\vee}(\mathfrak{su}(N))$].

Fundamental weights - From the set of simple roots $\{\boldsymbol{\alpha}^{(i)}\}$, we can introduce its dual, i.e., the fundamental weights $\boldsymbol{\omega}_{(i)}$ satisfying

$$\boldsymbol{\alpha}^{(i)\vee}.\boldsymbol{\omega}_{(j)} = \delta_j^i \,, \qquad (C5)$$

which can be used as the basis of the weights (<u>Dynkin basis</u>):

$$\boldsymbol{\mu} = \sum_{i=1}^{N-1} d(\boldsymbol{\mu})^i \, \boldsymbol{\omega}_{(j)} \,. \qquad (C6)$$

The coordinates $d(\boldsymbol{\mu})^i$ in this basis is called <u>Dynkin labels</u>. The lattice spanned by the basis $\{\boldsymbol{\omega}_{(i)}\}$ is called the <u>weight lattice</u> $\Lambda_{\mathrm{w}}(\mathfrak{su}(N))$ (see Fig. 15). The relation between the coroot lattice $\Lambda_{\mathrm{r}}^{\vee}(\mathfrak{su}(N))$ and the weight lattice $\Lambda_{\mathrm{w}}(\mathfrak{su}(N))$ is analogous to that between the lattices in the real space and the reciprocal space. Any irreducible representation $\mathcal{R}$ of $\mathfrak{su}(N)$ is specified by its highest weight $\boldsymbol{\lambda}_{\mathcal{R}}$ or its Dynkin labels $\{d(\mathcal{R})^i\}$

$$\boldsymbol{\lambda}_{\mathcal{R}} = \sum_{i=1}^{r} d(\mathcal{R})^i \boldsymbol{\omega}_{(j)} \quad (d^i \in \mathbb{Z}, d^i \geq 0) \qquad (C7)$$

and, by applying the lowering operators $E_{-\boldsymbol{\alpha}}$ ($\boldsymbol{\alpha} \in \Delta_+$), we can construct the corresponding irreducible representation (see Fig. 16 for $\mathfrak{su}(3)$ examples). In $\mathfrak{su}(N)$, the representation specified by $(d^1, d^2, \cdots, d^{N-1})$ has a Young diagram with d^1 columns with length 1, d^2 columns with length 2, $\cdots$, and d^{N-1} columns with length $N-1$. For example, the fundamental representations are always specified by the Dynkin

labels $\{d(\mathcal{R})^i\}$ in which only one of d^i is 1 and the others are zero.
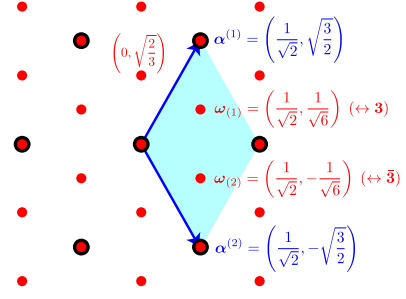
FIG. 15. (color online) The (co)root lattice $\Lambda_{\mathrm{r}}(\mathfrak{g})$ (black circles) and and the weight lattice $\Lambda_{\mathrm{w}}(\mathfrak{g})$ (red circles) of $\mathfrak{g} = \mathfrak{su}(3)$. The root (weight) lattice is an integer span of two simple (co)roots $\boldsymbol{\alpha}^{(1)}$ and $\boldsymbol{\alpha}^{(2)}$ (two fundamental weights $\boldsymbol{\omega}_{(1)}$ and $\boldsymbol{\omega}_{(2)}$). In $\mathfrak{su}(3)$, $\boldsymbol{\omega}_{(1)}$ and $\boldsymbol{\omega}_{(2)}$ respectively correspond to the highest weights of $\mathbf{3}$ and $\bar{\mathbf{3}}$.
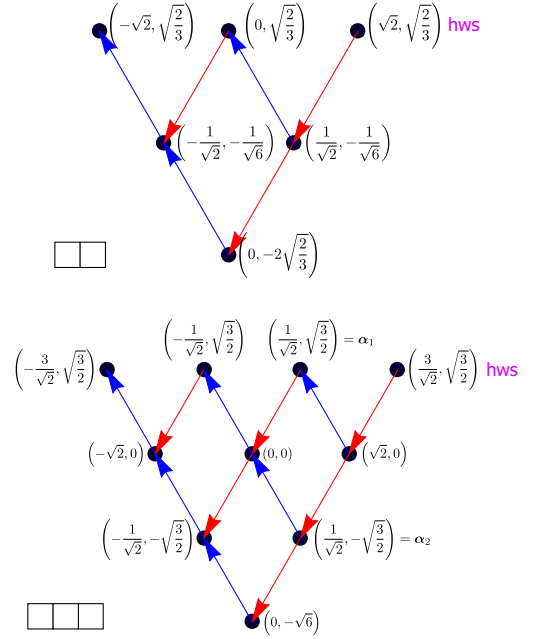
FIG. 16. (color online) Weights of $\mathbf{6}$ and $\mathbf{10}$-dimensional representations of $\mathfrak{su}(3)$. The representations $\mathbf{6}$ and $\mathbf{10}$ have highest weights (shown as "hws") with Dynkin labels $(d^1, d^2) = (2,0)$ and $(3,0)$, respectively. Red (blue) arrows show the action of the roots ("lowering operators") $-\boldsymbol{\alpha}^{(1)}$ $(-\boldsymbol{\alpha}^{(2)})$ to the weights (see Fig. 15 for the definitions of $\boldsymbol{\alpha}^{(1,2)}$).

2. Affine Lie Algebras and Wess-Zumino-Witten model

The affine Lie algebras are characterized by the following commutation relations which generalize (C1):

$$[J_n^{\alpha}, J_m^{\beta}] = if_{\alpha\beta\gamma}J_{n+m}^{\gamma} + \widetilde{k}n\delta_{m+n,0}\delta^{\alpha\beta} \qquad (C8)$$

(see, e.g., Refs. [46, 100] for physicist-friendly reviews of affine Lie algebras). Physically, (C8) is the algebra of the Fourier modes of the local SU(N) currents $\{J^\alpha(x)\}$ satisfying:

$$[\, J^\alpha(x)\, ,\, J^\beta(y)\,] = i\, f^{\alpha\beta\gamma} J^\gamma(y)\delta(x-y)$$
$$+ \frac{i}{2\pi}\widetilde{k}\,\delta^{\alpha\beta}\,\partial_x\delta(x-y) \quad \text{(C9)}$$
$$J^\alpha(x) = \frac{1}{L}\sum_{n\in\mathbb{Z}} e^{-i\frac{2\pi}{L}nx}\, J_n^\alpha\,.$$

The above are anomalous in that the right-hand side contains the central term [which is proportional to $\delta'(x)$] on top of the term expected from the Lie algebra. Obviously, the coefficient $\widetilde{k}$ of the central term depends on the normalization of J_n^α and it is convenient to introduce the normalization-independent integer k called the <u>level</u> of the affine Lie algebra by

$$\widetilde{k} = \frac{|\boldsymbol{\theta}|^2}{2}k\,,$$

where $|\boldsymbol{\theta}|$ is the length of the highest root (the quantization of k follows, e.g., from the consistency of the path-integral representation of the WZW model). The $|\boldsymbol{\theta}|$ depends on the normalization of the generators and, in $\mathfrak{su}(N)$, a convenient choice is to normalize the N-dimensional hermitian generators $\{J^\alpha\}$ as $\text{Tr}(J^\alpha J^\beta) = \delta^{\alpha\beta}$ which amounts to setting $|\boldsymbol{\theta}| = \sqrt{2}$. Then, we do not have to distinguish between the coefficient $\widetilde{k}$ of the central term and the level $k\,(\in\mathbb{Z})$. The special case $m = n = 0$ of (C8) reduces to (C1), which means that the zero modes $\{J_0^\alpha\}$ form the usual $\mathfrak{su}(N)$ Lie algebra (called the <u>horizontal subalgebra</u>).

As a class of CFT with Lie-algebra symmetry, the WZW CFT has the Virasoro generators $\{L_n\}$ which are bilinear in J_n^α (<u>Sugawara form</u>) [100, 101]:

$$L_n = \frac{1}{|\boldsymbol{\theta}|^2(g^\vee + k)}\sum_\alpha\sum_{m\in\mathbb{Z}} :J_m^\alpha J_{n-m}^\alpha:\,, \quad \text{(C10)}$$

where the normal-ordering $:\cdots:$ is defined by

$$:J_m^\alpha J_n^\alpha: = \begin{cases} J_m^\alpha J_n^\alpha & \text{when } m < 0 \\ J_n^\alpha J_m^\alpha & \text{when } m \geq 0\,. \end{cases}$$

The number $g^\vee$ (the <u>dual Coxter number</u>), which is peculiar to a given Lie algebra, is given by the structure constants as $-f^{\alpha\beta\mu}f^{\alpha\mu\gamma} = |\boldsymbol{\theta}|^2 g^\vee \delta^{\beta\gamma}$ and is equal to N in $\mathfrak{su}(N)$. By a direct calculation, we can show that the above $\{L_n\}$ satisfy the Virasoro algebra

$$[L_m, L_n] = (m-n)L_{m+n} + \frac{1}{12}c(\mathfrak{g},k)m(m^2-1)\delta_{m+n,0} \quad \text{(C11)}$$

with the central charge given by

$$c(\mathfrak{g},k) = \frac{k\,\dim(\mathfrak{g})}{k + g^\vee} \quad (k = 1, 2, \ldots)\,, \quad \text{(C12)}$$

which, for $\mathfrak{su}(N)$, reads

$$c(\mathfrak{su}(N),k) = \frac{k(N^2-1)}{N + k}\,. \quad \text{(C13)}$$

On top of Eq. (C11), $\{L_n\}$ satisfy the following commutation relations with the generators $\{J_n^\alpha\}$:

$$[L_m, J_n^\alpha] = -n J_{m+n}^\alpha\,. \quad \text{(C14)}$$

In particular,

$$[L_0, J_n^\alpha] = -n J_n^\alpha\,, \quad [L_0, J_0^\alpha] = 0 \quad \text{(C15)}$$

implies that not only L_{-n} ($n > 0$) but also J_{-n}^α increase the eigenvalue of L_0 and that for each eigenvalue of L_0 (i.e., for each level of conformal towers) we have a <u>reducible</u> representation of $\mathfrak{su}(N)$ (formed by $\{J_0^\alpha\}$).

In CFTs with extended symmetries, it is convenient to define the <u>primary states</u> $|\phi\rangle$ as those annihilated by all J_n^α with positive n:

$$J_n^\alpha|\phi\rangle = 0 \quad (n > 0)\,. \quad \text{(C16)}$$

Then, from (C10), $|\phi\rangle$ <u>automatically</u> satisfy the primary condition with respect to the Virasoro algebra [the converse is not true; in that sense, (C16) is stronger than (C17)]:

$$L_n|\phi\rangle = 0 \quad (n > 0)$$
$$L_0|\phi\rangle = \frac{1}{|\boldsymbol{\theta}|^2(g^\vee + k)}\sum_\alpha J_0^\alpha J_0^\alpha|\phi\rangle \quad \text{(C17)}$$
$$= \frac{1}{|\boldsymbol{\theta}|^2(g^\vee + k)}\mathcal{C}_2|\phi\rangle = h_\phi|\phi\rangle\,,$$

where J_ϕ^α is a matrix representation of J^α and $\mathcal{C}_2$ is the quadratic Casimir of $\mathfrak{su}(N)$. All these mean that the primary states of the WZW model transform under the irreducible representations $\mathcal{R}$ of the ordinary $\mathfrak{su}(N)$ spanned by the subset $\{J_0^\alpha\}$:

$$|\phi\rangle = |\mathcal{R}; \boldsymbol{\mu}(\mathcal{R})\rangle \quad (\boldsymbol{\mu}(\mathcal{R}): \text{ weights of } \mathcal{R})$$
$$J_0^\alpha|\mathcal{R}; \boldsymbol{\mu}(\mathcal{R})\rangle = -J^\alpha(\mathcal{R})|\mathcal{R}; \boldsymbol{\mu}(\mathcal{R})\rangle \quad \text{(C18)}$$
$$[J^\alpha(\mathcal{R}): J^\alpha \text{ in representation } \mathcal{R}]$$

and that the conformal weights h_ϕ are given essentially by the quadratic Casimir $\mathcal{C}_2$ of $\mathcal{R}$:

$$h(\mathcal{R}) = \frac{\mathcal{C}_2(\mathcal{R})}{|\boldsymbol{\theta}|^2(g^\vee + k)} \quad (g^\vee = N \text{ for } \mathfrak{su}(N))\,. \quad \text{(C19)}$$

As in other CFTs, these are the lowest states in a given $\mathcal{R}$-sector and the higher-lying states are generated by applying J_{-n}^α ($n > 0$).

There is a selection rule about the allowed $\mathcal{R}$ for a given level k, which, in terms of the Dynkin labels $(d^1, \ldots, d^r)$ [see Eq. (C7)], reads for $\mathfrak{su}(N)$

$$\sum_{i=1}^{N-1} d(\mathcal{R})^i \leq k\,. \quad \text{(C20)}$$

In the level-1 ($k = 1$) SU(N) WZW model which is relevant in this paper, only the vacuum [$\mathbf{1}$; SU(N)-singlet with $\boldsymbol{d} = (0, \ldots, 0)$] and the $N - 1$ antisymmetric representations aIR$_N(r_0)$ [rank-r_0 antisymmetric tensor with $\boldsymbol{d} = (0, \ldots, 0, \underbrace{1}_{r_0}, 0, \ldots, 0)$; $r_0 = 1, \ldots, N - 1$] in Sec. II C are allowed for primary states:

$$
\begin{aligned}
\mathcal{C}_2\left(r_0\{\boxed{}\}\right) &= \frac{N+1}{2N} r_0(N - r_0)|\boldsymbol{\theta}|^2 \\
h\left(r_0\{\boxed{}\}\right) &= \frac{1}{2N} r_0(N - r_0) \quad (r_0 = 0, \ldots, N - 1) \, .
\end{aligned}
\tag{C21}
$$

These N different primary states (fields) correspond to N topologically degenerate ground states of SU(N)$_1$ CSL on a torus. For the selection rule for general $\mathfrak{g}$, see, e.g., Sec. 3.4 of Ref. [100].

3. Finite-size spectrum

For the clarity of the explanation, we assume $\mathfrak{g} = \mathfrak{su}(N)$ and normalize the generator as $|\boldsymbol{\theta}| = \sqrt{2}$ in this section. In this normalization, the coefficient $\tilde{k}$ of the central term is equal to the level k, and $\mathcal{C}_2$ is given simply by

$$
\begin{aligned}
\mathcal{C}_2(\mathcal{R}) &= \sum_{i,j=1}^{N-1} (\boldsymbol{d}(\mathcal{R}) + \boldsymbol{e})_i (A^{-1})^{ij} (\boldsymbol{d}(\mathcal{R}) + \boldsymbol{e})_j \\
&\quad - \frac{1}{12} N(N^2 - 1) \, , \\
\boldsymbol{e} &\equiv \underbrace{(1, 1, \ldots, 1)}_{N-1} \, ,
\end{aligned}
\tag{C22}
$$

where the matrix A is the Cartan matrix defined in (C4) and $\boldsymbol{d}(\mathcal{R})$ is the Dynkin labels that characterizes the highest weight $\boldsymbol{\lambda}_{\mathcal{R}}$ of the representation $\mathcal{R}$ by Eq. (C7). When we normalize the N-dimensional generators as $\text{Tr}(J^\alpha J^\beta) = \kappa \delta^{\alpha\beta}$, we need to multiply the right-hand side by κ.

The Hamiltonian of the chiral CFT is given by [46, 102]:

$$
H_{\text{chiral}} = \frac{2\pi}{l} v \left(L_0 - \frac{c}{24}\right) \quad (l : \text{system size}) \, ,
\tag{C23}
$$

where v is the velocity parameter of the system. As L_0 and c in the level-k SU(N) WZW CFT are given respectively by (C10) and (C13), we obtain:

$$
\begin{aligned}
H_{\text{chiral}}^{\mathfrak{su}(N)} &= \frac{2\pi v}{l} \frac{1}{2(N+k)} \sum_{\alpha \in \text{SU}(N)} \left\{ J_0^\alpha J_0^\alpha + 2 \sum_{n=1}^\infty J_{-n}^\alpha J_n^\alpha \right\} \\
&\quad - \frac{\pi v}{12l} \frac{(N^2 - 1)k}{N + k} \, .
\end{aligned}
\tag{C24}
$$

The results in the previous section show that the Hilbert space in the sector specified by an irreducible representation $\mathcal{R}$ of $\mathfrak{su}(N)$ [$\mathcal{R}$ obeys the selection rule (C20)] consists of the ground (lowest) states with energy

$$
\frac{2\pi v}{l} \frac{\mathcal{C}_2(\mathcal{R})}{2(N+k)} - \frac{\pi v}{12l} \frac{(N^2 - 1)k}{N + k}
$$

and the equally-spaced excited states (with the level spacing $2\pi/l$). All these states are labeled by the eigenvalues of L_0 (energy) and $\{H_0^1, \ldots, H_0^{N-1}\}$ (weight $\boldsymbol{\mu}$ of horizontal subalgebra $\{J_0^\alpha\}$). As the action of the $\mathfrak{su}(N)$-generators J_0^α does not change the value of L_0 (i.e., energy) [see Eq. (C15)], each excited level decomposes into a direct sum of several irreducible representations of $\mathfrak{su}(N)$ (TABLES IV–C 3 shown below give such decompositions).

There is a compact way of encoding the information on the structure (i..e., energy, degeneracy, and the Lie-algebraic structure) of the Hilbert space of the WZW CFT. Consider the finite-temperature (T) partition function of the system:

$$
\begin{aligned}
Z &= \text{Tr}_{\mathcal{R}} \, e^{-\frac{2\pi}{Tl} v\left(L_0 - \frac{c}{24}\right)} = q^{-\frac{c}{24}} \text{Tr}_{\mathcal{R}} \, q^{L_0} \equiv Z_{\mathcal{R}}(q) \\
&(q \equiv e^{-\frac{2\pi}{Tl} v}) \, ,
\end{aligned}
\tag{C25}
$$

where the subscript $\mathcal{R}$ means that the trace is taken over all the excited states within the $\mathcal{R}$-sector. Since L_0 takes values $h(\mathcal{R}) + N$ (with N being non-negative integers), if we expand $Z_{\mathcal{R}}(q)$ in a power-series

$$
Z_{\mathcal{R}}(q) = q^{h(\mathcal{R}) - \frac{c}{24}} \sum_{N=0}^\infty D(N) q^N \, ,
\tag{C26}
$$

it immediately gives the degeneracy $D(N)$ of the N-th excited state.

In order to know the Lie-algebraic structure, it is convenient to introduce the "fugacities" $\{z_i\}$ for the weight and consider the following generalized partition function:

$$
\widetilde{Z}_{\mathcal{R}}(q; \{z_i\}) = q^{-\frac{c}{24}} \text{Tr}_{\mathcal{R}} \left\{ q^{L_0} \prod_{i=1}^{N-1} z_i^{H_0^i} \right\} \, ,
\tag{C27}
$$

where $\prod_i$ is over all the $N - 1$ Cartan generators $\{H_0^i\}$ of the $\mathfrak{su}(N)$ subalgebra $\{J_0^\alpha\}$. Now the coefficient of $q^{N+h(\mathcal{R}) - \frac{c}{24}}$ is a polynomial of $z_1^{\mu_1} z_2^{\mu_2} \cdots z_{N-1}^{\mu_{N-1}}$ that gives the multiplicity of the weight $\boldsymbol{\mu}$ in the N-th excited level. In fact, the generalized partition function $\widetilde{Z}_{\mathcal{R}}(T, L)$ is nothing but the character of the affine Lie algebra and its expression using the generalized theta function is known explicitly (see, e.g., section 14.4 of Ref. [46] for more details). TABLES IV–C 3, which show the contents of irreducible representations appearing at the excited levels of a given $\mathcal{R}$-sector, are obtained in this manner. For example, TABLE V shows the structure of the Hilbert space of the level-1 SU(2) WZW CFT in the sector of spin-1/2 representation [$h(j = 1/2) = 1/4$] and "Order" denotes q^{L_0}. The degeneracy 2 of the first entry ($q^{1/4}$) is a direct consequence of the doublet level (primary states) constitutes the $j = 1/2$ representation of $\mathfrak{su}(2)$. The third entry from the top implies that the second excited level ($q^{9/4} = q^{1/4+2}$) is

six-fold degenerate and decomposes into one $j = 1/2$ ($\square$) and one $j = 3/2$ ($\square\square\square$) representations:

$$\mathbf{2}(\square) \oplus \mathbf{4}(\square\square\square) \ .$$

For level-1 $\mathfrak{su}(N)$ WZW CFT (for level-1 simply-laced $\mathfrak{g}$, in general), there is a simple way of constructing the Hilbert space in terms of $N-1$ (i.e., rank-$\mathfrak{g}$) free bosons (Frenkel-Kac construction). First we note that the central charge (C13) of level-1 ($k = 1$) $\mathfrak{su}(N)$ WZW CFT is $c = N-1$, which clearly suggests its close relation to a system of $N-1$ free bosons. Below, we quickly sketch how we derive the partition function of the $\mathrm{SU}(N)_1$ WZW CFT. To begin with, we prepare a set of $N-1$ bosons $\phi_i(z)$ ($i = 1, \ldots, N-1$) which are normalized as:

$$\langle \phi_i(z)\phi_j(w) \rangle \sim -\delta_{ij} \log(z-w) \ . \tag{C28}$$

The key properties of these bosons are the following operator-product expansions (OPE) [46, 102]:

$$\partial_z \phi_i(z)\partial_w \phi_j(w) \sim \frac{-\delta_{ij}}{(z-w)^2}$$

$$\partial_z \phi_i(z) : e^{i\boldsymbol{v}\cdot\boldsymbol{\phi}(w)} := \partial_z \phi_i(z) : e^{i\sum_j v_j \phi_j(w)} :$$

$$\sim \frac{-iv_i}{z-w} : e^{i\boldsymbol{v}\cdot\boldsymbol{\phi}(w)} :$$

$$T(z) : e^{i\boldsymbol{v}\cdot\boldsymbol{\phi}(w)} :$$

$$= -\frac{1}{2}\sum_{i=1}^{N-1} : (\partial_z \phi_i(z))^2 : e^{i\boldsymbol{v}\cdot\boldsymbol{\phi}(w)} :$$

$$\sim \frac{\boldsymbol{v}^2/2}{(z-w)^2} : e^{i\boldsymbol{v}\cdot\boldsymbol{\phi}(w)} : + \frac{1}{z-w}\partial_w : e^{i\boldsymbol{v}\cdot\boldsymbol{\phi}(w)} : + \cdots \ , \tag{C29}$$

where $\boldsymbol{v} = (v_1, \ldots, v_{N-1})$ and $\boldsymbol{\phi} = (\phi_1, \ldots, \phi_{N-1})$. Therefore, if we identify

$$H^i(z) = i\partial_z \phi_i(z) \ , \quad E^{\boldsymbol{\alpha}}(z) =: e^{i\boldsymbol{\alpha}\cdot\boldsymbol{\phi}(w)} : \tag{C30}$$

(all the roots $\boldsymbol{\alpha}$ have the length $|\boldsymbol{\alpha}| = \sqrt{2}$), they satisfy the OPEs expected for the generators of $k = 1$ $\mathfrak{su}(N)$ (with scaling dimension 1) [46, 100]:

$$H^i(z)H^j(w) \sim \frac{\delta_{ij}}{(z-w)^2}$$

$$H^i(z)E^{\boldsymbol{\alpha}}(w) \sim \frac{\alpha_i}{z-w}E_{\boldsymbol{\alpha}}(w)$$

$$E^{\boldsymbol{\alpha}}(z)E^{\boldsymbol{\beta}}(w)$$

$$\sim (z-w)^{\boldsymbol{\alpha}\cdot\boldsymbol{\beta}}E^{\boldsymbol{\alpha}+\boldsymbol{\beta}}(w)$$

$$+ i(z-w)^{\boldsymbol{\alpha}\cdot\boldsymbol{\beta}+1}\boldsymbol{\alpha}\cdot\partial_w\boldsymbol{\phi}(w)E^{\boldsymbol{\alpha}+\boldsymbol{\beta}}(w) \tag{C31}$$

[in $\mathfrak{su}(N)$ with $|\boldsymbol{\alpha}| = \sqrt{2}$, $\boldsymbol{\alpha}\cdot\boldsymbol{\beta} = -1$ when $\boldsymbol{\alpha} + \boldsymbol{\beta}$ is a root and $\boldsymbol{\alpha} \neq -\boldsymbol{\beta}$, and $\boldsymbol{\alpha}\cdot\boldsymbol{\beta} = -2$ when $\boldsymbol{\alpha} = -\boldsymbol{\beta}$]. This suggests that we can construct the Hilbert space of the $k =$

1 $\mathrm{SU}(N)$ WZW CFT by applying $H^i(z) = i\partial_z\phi_i(z)$ ($i = 1, \ldots, N-1$) repeatedly to the bosonic primary states $|\boldsymbol{\mu}\rangle \equiv |\mu_1, \ldots, \mu_{N-1}\rangle =: e^{i\boldsymbol{\mu}\cdot\boldsymbol{\phi}(0)} : |0\rangle$ [with $\boldsymbol{\mu}$ being the weights of $\mathfrak{su}(N)$], that has the eigenvalue $L_0|\boldsymbol{\mu}\rangle = \boldsymbol{\mu}^2/2|\boldsymbol{\mu}\rangle$. The summation over all the possible excited states (with the mode $E_n = (2\pi/l)n$ being occupied with N_n bosons) of the i-th linearly-dispersive boson above the primary state $|\boldsymbol{\mu}\rangle$ yields the partial partition function

$$e^{-\frac{2\pi v}{Tl}\frac{1}{2}\mu_i^2}z_i^{\mu_i}\prod_{n=1}^{\infty}\left\{\sum_{N_n=0}^{\infty}e^{-\frac{2\pi v}{Tl}nN_n}\right\} = q^{\frac{1}{2}\mu_i^2}z_i^{\mu_i}/\prod_{n=1}^{\infty}(1-q^n) \ ,$$

which is to be combined together for all $N-1$ bosons yielding $q^{\frac{1}{2}\boldsymbol{\mu}^2}\prod_{i=1}^{N-1}z_i^{\mu_i}\prod_{n=1}^{\infty}(1-q^n)^{N-1}$. As the application of the other generators $E^{\boldsymbol{\alpha}}(z)$ changes the "weight" of the primary states as $|\boldsymbol{\mu}\rangle \to |\boldsymbol{\mu}+\boldsymbol{\alpha}\rangle$, all these bosonic conformal towers specified by weights $\boldsymbol{\mu}$ that are related to each other by translation by $\boldsymbol{\alpha}$ must be regarded as belonging to the same WZW conformal tower. In $\mathfrak{su}(3)$, for instance, the weights $\boldsymbol{\mu}$ on the root lattice all together constitute a single WZW tower of the identity representation $\mathbf{1}$ (see Fig. 15). Summing up the partial partition functions for those "equivalent" $\boldsymbol{\mu}$, we obtain the partition function of $k = 1$ $\mathrm{SU}(N)$ WZW CFT (see section 15.6 of Ref. [46] for more details):

$$\widetilde{Z}_{\mathcal{R}}(q; \{z_i\})$$

$$\equiv \frac{q^{-\frac{N-1}{24}}}{\prod_{n=1}^{\infty}(1-q^n)^{N-1}}\left\{\sum_{\boldsymbol{\mu}\in\boldsymbol{\lambda}_{\mathcal{R}}+\Lambda_{\mathrm{r}}}q^{\frac{1}{2}\boldsymbol{\mu}^2}\left(\prod_{i=1}^{N-1}z_i^{\mu_i}\right)\right\} \ , \tag{C32}$$

where $\boldsymbol{\lambda}_{\mathcal{R}}$ is the highest weight of the representation $\mathcal{R}$ and the summation is taken over all the points $\boldsymbol{\mu}$ of the weight lattice Λ_{w} which are equivalent to $\boldsymbol{\lambda}_{\mathcal{R}}$ modulo the root lattice Λ_{r} spanned by the simple roots $\{\boldsymbol{\alpha}^{(i)}\}$. Since such $\boldsymbol{\mu}$ are given explicitly as

$$\boldsymbol{\mu} = \boldsymbol{\lambda}_{\mathcal{R}} + \sum_{i=1}^{N-1}n_i\boldsymbol{\alpha}^{(i)} \ , \tag{C33}$$

we can trade the sum over $\boldsymbol{\mu} \in \boldsymbol{\lambda}_{\mathcal{R}} + \Lambda_{\mathrm{r}}$ with that over the $N-1$ integers $\{n_i\}$. By construction, the representations $\mathcal{R}$ allowed as primary in the $\mathrm{SU}(N)_1$ WZW CFT, which is relevant in this paper, are restricted to the points of Λ_{w} within the unit cell of Λ_{r}. As all those $\mathcal{R}$ have the Dynkin labels $\sum_{i=1}^{N-1}d(\mathcal{R})^i = 0, 1$, this selection rule is consistent with the general one (C20). For instance, in order to obtain the partition function for $\mathcal{R} = \mathbf{3}$ ($\square$) of $\mathfrak{su}(3)$, we sum over all the red points in Fig. 15 connected to the point $\boldsymbol{\omega}_{(1)}$ (i.e., the highest weight of $\mathbf{3}$) by the translation generated by two simple roots $\boldsymbol{\alpha}^{(1)}$ and $\boldsymbol{\alpha}^{(2)}$ (red and blue arrows, respectively); the three inequivalent points in the hatched "unit cell" correspond to the three primary fields $\phi_{\mathbf{1}}$ (singlet vacuum), $\phi_{\mathbf{3}}$, and $\phi_{\bar{\mathbf{3}}}$ allowed in level-1 $\mathfrak{su}(3)$.

TABLE IV. $SU(2)_1$ WZW model – Tower of states starting from $\overset{1}{\bullet}$.

L_0	Order	Irreps / Multiplicities
0	q^0	$1\ \overset{1}{\bullet}$
1	q^1	$1\ \overset{3}{\square\square}$
2	q^2	$1\ \overset{1}{\bullet} \oplus 1\ \overset{3}{\square\square}$
3	q^3	$1\ \overset{1}{\bullet} \oplus 2\ \overset{3}{\square\square}$
4	q^4	$2\ \overset{1}{\bullet} \oplus 2\ \overset{3}{\square\square} \oplus 1\ \overset{5}{\square\square\square\square}$
5	$q^5 5$	$2\ \overset{1}{\bullet} \oplus 4\ \overset{3}{\square\square} \oplus 1\ \overset{5}{\square\square\square\square}$
6	q^6	$4\ \overset{1}{\bullet} \oplus 5\ \overset{3}{\square\square} \oplus 2\ \overset{5}{\square\square\square\square}$
7	q^7	$4\ \overset{1}{\bullet} \oplus 8\ \overset{3}{\square\square} \oplus 3\ \overset{5}{\square\square\square\square}$

TABLE V. $SU(2)_1$ WZW model – Tower of states starting from $\overset{2}{\square}$.

L_0	Order	Irreps / Multiplicities
0	$q^{1/4}$	$1\ \overset{2}{\square}$
1	$q^{5/4}$	$1\ \overset{2}{\square}$
2	$q^{9/4}$	$1\ \overset{2}{\square} \oplus 1\ \overset{4}{\square\square\square}$
3	$q^{13/4}$	$2\ \overset{2}{\square} \oplus 1\ \overset{4}{\square\square\square}$
4	$q^{17/4}$	$3\ \overset{2}{\square} \oplus 2\ \overset{4}{\square\square\square}$
5	$q^{21/4}$	$4\ \overset{2}{\square} \oplus 3\ \overset{4}{\square\square\square}$
6	$q^{25/4}$	$6\ \overset{2}{\square} \oplus 4\ \overset{4}{\square\square\square} \oplus 1\ \overset{6}{\square\square\square\square\square}$
7	$q^{29/4}$	$8\ \overset{2}{\square} \oplus 6\ \overset{4}{\square\square\square} \oplus 1\ \overset{6}{\square\square\square\square\square}$

TABLE VI. SU(3)$_1$ WZW model – Tower of states starting from $\mathbf{1}$ (•).

L_0	Order	Irreps / Multiplicities
0	q^0	$1\;\mathbf{1}$
1	q^1	$1\;\mathbf{8}$
2	q^2	$1\;\mathbf{1} \oplus 2\;\mathbf{8}$
3	q^3	$2\;\mathbf{1} \oplus 3\;\mathbf{8} \oplus 1\;\mathbf{10} \oplus 1\;\overline{\mathbf{10}}$
4	q^4	$3\;\mathbf{1} \oplus 6\;\mathbf{8} \oplus 1\;\mathbf{10} \oplus 1\;\overline{\mathbf{10}} \oplus 1\;\mathbf{27}$
5	q^5	$4\;\mathbf{1} \oplus 10\;\mathbf{8} \oplus 3\;\mathbf{10} \oplus 3\;\overline{\mathbf{10}} \oplus 2\;\mathbf{27}$
6	q^6	$8\;\mathbf{1} \oplus 16\;\mathbf{8} \oplus 5\;\mathbf{10} \oplus 5\;\overline{\mathbf{10}} \oplus 5\;\mathbf{27}$
7	q^7	$10\;\mathbf{1} \oplus 27\;\mathbf{8} \oplus 9\;\mathbf{10} \oplus 9\;\overline{\mathbf{10}} \oplus 8\;\mathbf{27} \oplus 1\;\overline{\mathbf{35}} \oplus 1\;\mathbf{35}$

TABLE VII. SU(3)$_1$ WZW model – Tower of states starting from $\mathbf{3}$ (resp. $\overline{\mathbf{3}}$ by conjugation of all IRREPs).

L_0	Order	Irreps / Multiplicities
0	$q^{1/3}$	$1\;\mathbf{3}$
1	$q^{4/3}$	$1\;\mathbf{3} \oplus 1\;\overline{\mathbf{6}}$
2	$q^{7/3}$	$2\;\mathbf{3} \oplus 1\;\overline{\mathbf{6}} \oplus 1\;\mathbf{15}$
3	$q^{10/3}$	$3\;\mathbf{3} \oplus 3\;\overline{\mathbf{6}} \oplus 2\;\mathbf{15}$
4	$q^{13/3}$	$6\;\mathbf{3} \oplus 4\;\overline{\mathbf{6}} \oplus 4\;\mathbf{15} \oplus 1\;\mathbf{24}$
5	$q^{16/3}$	$9\;\mathbf{3} \oplus 8\;\overline{\mathbf{6}} \oplus 1\;\mathbf{15'} \oplus 7\;\mathbf{15} \oplus 2\;\mathbf{24}$
6	$q^{19/3}$	$15\;\mathbf{3} \oplus 12\;\overline{\mathbf{6}} \oplus 1\;\mathbf{15'} \oplus 13\;\mathbf{15} \oplus 4\;\mathbf{24} \oplus 1\;\mathbf{42}$
7	$q^{22/3}$	$22\;\mathbf{3} \oplus 21\;\overline{\mathbf{6}} \oplus 3\;\mathbf{15'} \oplus 21\;\mathbf{15} \oplus 8\;\mathbf{24} \oplus 2\;\mathbf{42}$

TABLE VIII. SU(4)$_1$ WZW model – Tower of states starting from $\mathbf{1}$ (•).
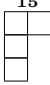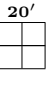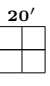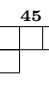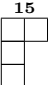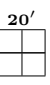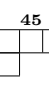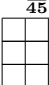
L_0	Order	Irreps / Multiplicities
0	q^0	**1** $\mathbf{1}$(•)
1	q^1	**1** $\mathbf{15}$
2	q^2	**1** $\mathbf{1}$(•) $\oplus$ **2** $\mathbf{15}$ $\oplus$ **1** $\mathbf{20'}$
3	q^3	**2** $\mathbf{1}$(•) $\oplus$ **4** $\mathbf{15}$ $\oplus$ **1** $\mathbf{20'}$ $\oplus$ **1** $\mathbf{45}$ $\oplus$ **1** $\overline{\mathbf{45}}$
4	q^4	**4** $\mathbf{1}$(•) $\oplus$ **7** $\mathbf{15}$ $\oplus$ **4** $\mathbf{20'}$ $\oplus$ **2** $\mathbf{45}$ $\oplus$ **2** $\overline{\mathbf{45}}$ $\oplus$ **1** $\mathbf{84}$

TABLE IX. SU(4)$_1$ WZW model – Tower of states starting from $\mathbf{4}$ (resp. $\overline{\mathbf{4}}$ by conjugation of all IRREPs).
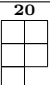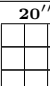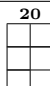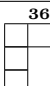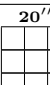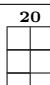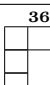
L_0	Order	Irreps / Multiplicities
0	$q^{3/8}$	**1** $\mathbf{4}$
1	$q^{11/8}$	**1** $\mathbf{4}$ $\oplus$ **1** $\mathbf{20}$
2	$q^{19/8}$	**2** $\mathbf{4}$ $\oplus$ **2** $\mathbf{20}$ $\oplus$ **1** $\mathbf{36}$
3	$q^{27/8}$	**4** $\mathbf{4}$ $\oplus$ **1** $\mathbf{20''}$ $\oplus$ **4** $\mathbf{20}$ $\oplus$ **2** $\mathbf{36}$ $\oplus$ **1** $\mathbf{60}$
4	$q^{35/8}$	**7** $\mathbf{4}$ $\oplus$ **1** $\mathbf{20''}$ $\oplus$ **8** $\mathbf{20}$ $\oplus$ **5** $\mathbf{36}$ $\oplus$ **2** $\mathbf{60}$ $\oplus$ **1** $\mathbf{140}$

TABLE X. SU(4)$_1$ WZW model – Tower of states starting from $\square$ (**6**).

L_0	Order	Irreps / Multiplicities
0	$q^{1/2}$	**1** (**6**)
1	$q^{3/2}$	**1** (**6**) $\oplus$ **1** (**10**) $\oplus$ **1** ($\overline{\mathbf{10}}$)
2	$q^{5/2}$	**3** (**6**) $\oplus$ **1** (**10**) $\oplus$ **1** ($\overline{\mathbf{10}}$) $\oplus$ **1** (**64**)
3	$q^{7/2}$	**4** (**6**) $\oplus$ **3** (**10**) $\oplus$ **3** ($\overline{\mathbf{10}}$) $\oplus$ **3** (**64**)
4	$q^{9/2}$	**9** (**6**) $\oplus$ **5** (**10**) $\oplus$ **5** ($\overline{\mathbf{10}}$) $\oplus$ **1** (**50**) $\oplus$ **6** (**64**) $\oplus$ **1** ($\overline{\mathbf{70}}$) $\oplus$ **1** (**70**)

TABLE XI. SU(5)$_1$ WZW model – Tower of states starting from $\bullet$ (**1**).

L_0	Order	Irreps / Multiplicities
0	q^0	**1** (**1**, $\bullet$)
1	q^1	**1** (**24**)
2	q^2	**1** (**1**, $\bullet$) $\oplus$ **2** (**24**) $\oplus$ **1** (**75**)
3	q^3	**2** (**1**, $\bullet$) $\oplus$ **4** (**24**) $\oplus$ **2** (**75**) $\oplus$ **1** (**126**) $\oplus$ **1** ($\overline{\mathbf{126}}$)

TABLE XII. SU(5)$_1$ WZW model – Tower of states starting from ▢ (resp. ⬒ $\overline{\mathbf{5}}$ by conjugation of all IRREPs).

L_0	Order	Irreps / Multiplicities
0	$q^{2/5}$	**1** $\mathbf{5}$
1	$q^{7/5}$	**1** $\mathbf{5}$ $\oplus$ **1** $\mathbf{45}$
2	$q^{12/5}$	**2** $\mathbf{5}$ $\oplus$ **2** $\mathbf{45}$ $\oplus$ **1** $\mathbf{50}$ $\oplus$ **1** $\mathbf{70}$
3	$q^{17/5}$	**4** $\mathbf{5}$ $\oplus$ **5** $\mathbf{45}$ $\oplus$ **1** $\mathbf{50}$ $\oplus$ **2** $\mathbf{70}$ $\oplus$ **1** $\mathbf{105}$ $\oplus$ **1** $\mathbf{280}$

TABLE XIII. SU(5)$_1$ WZW model – Tower of states starting from ⬒ $\mathbf{10}$ (resp. ⬒ $\overline{\mathbf{10}}$ by conjugation of all IRREPs).

L_0	Order	Irreps / Multiplicities
0	$q^{3/5}$	**1** $\mathbf{10}$
1	$q^{8/5}$	**1** $\mathbf{10}$ $\oplus$ **1** $\mathbf{15}$ $\oplus$ **1** $\mathbf{40}$
2	$q^{13/5}$	**3** $\mathbf{10}$ $\oplus$ **1** $\mathbf{15}$ $\oplus$ **2** $\mathbf{40}$ $\oplus$ **1** $\mathbf{175}$
3	$q^{18/5}$	**5** $\mathbf{10}$ $\oplus$ **3** $\mathbf{15}$ $\oplus$ **1** $\mathbf{35}$ $\oplus$ **4** $\mathbf{40}$ $\oplus$ **3** $\mathbf{175}$ $\oplus$ **1** $\mathbf{210}$

TABLE XIV. SU(6)₁ WZW model – Tower of states starting from $\overset{\mathbf{1}}{\bullet}$.
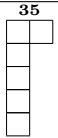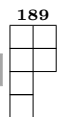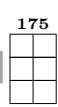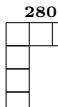
TABLE XV. SU(6)₁ WZW model – Tower of states starting from $\overset{\mathbf{6}}{\square}$ (resp. $\overset{\overline{\mathbf{6}}}{\square}$ by conjugation of all IRREPs.
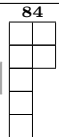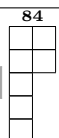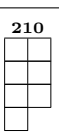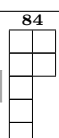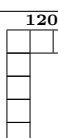
TABLE XVI. SU(6)$_1$ WZW model – Tower of states starting from ▯ (resp. ▯ by conjugation of all IRREPs).

TABLE XVII. SU(7)$_1$ WZW model – Tower of states starting from **1**•.

TABLE XVIII. SU(7)$_1$ WZW model – Tower of states starting from ▯ (resp. ▯ by conjugation of all IRREPs).

L_0	Order	Irreps / Multiplicities
0	$q^{3/7}$	**1** **7**
1	$q^{10/7}$	**1** **7** ⊕ **1** **140**
2	$q^{17/7}$	**2** **7** ⊕ **2** **140** ⊕ **1** **189** ⊕ **1** **588**
3	$q^{24/7}$	**4** **7** ⊕ **5** **140** ⊕ **2** **189** ⊕ **1** **490′** ⊕ **2** **588** ⊕ **1** **840** ⊕ **1** **2016**

TABLE XIX. SU(7)$_1$ WZW model – Tower of states starting from ▯ (resp. ▯ by conjugation of all IRREPs).

L_0	Order	Irreps / Multiplicities
0	$q^{5/7}$	**1** **21**
1	$q^{12/7}$	**1** **21** ⊕ **1** **28** ⊕ **1** **224**
2	$q^{19/7}$	**3** **21** ⊕ **1** **28** ⊕ **2** **224** ⊕ **1** **490** ⊕ **1** **735**
3	$q^{26/7}$	**5** **21** ⊕ **3** **28** ⊕ **5** **224** ⊕ **2** **490** ⊕ **3** **735** ⊕ **1** **756** ⊕ **1** **3402**

TABLE XX. SU(7)$_1$ WZW model – Tower of states starting from ☐ (resp. ☐ **35** by conjugation of all IRREPs).

L_0	Order	Irreps / Multiplicities
0	q	$1\cdot\mathbf{35}$
1	q	$1\cdot\mathbf{35} \oplus 1\cdot\mathbf{112} \oplus 1\cdot\mathbf{210}$
2	q	$3\cdot\mathbf{35} \oplus 2\cdot\mathbf{112} \oplus 1\cdot\mathbf{196} \oplus 2\cdot\mathbf{210} \oplus 1\cdot\mathbf{1323}$
3	q	$6\cdot\mathbf{35} \oplus 1\cdot\mathbf{84} \oplus 4\cdot\mathbf{112} \oplus 1\cdot\mathbf{196} \oplus 5\cdot\mathbf{210} \oplus 1\cdot\mathbf{378} \oplus 1\cdot\mathbf{1260} \oplus 3\cdot\mathbf{1323} \oplus 1\cdot\mathbf{3024}$

TABLE XXI. SU(8)$_1$ WZW model – Tower of states starting from $\overset{\mathbf{1}}{\bullet}$.

L_0	Order	Irreps / Multiplicities
0	q^0	$1\cdot\overset{\mathbf{1}}{\bullet}$
1	q^1	$1\cdot\mathbf{63}$
2	q^2	$1\cdot\overset{\mathbf{1}}{\bullet} \oplus 2\cdot\mathbf{63} \oplus 1\cdot\mathbf{720}$
3	q^3	$2\cdot\overset{\mathbf{1}}{\bullet} \oplus 4\cdot\mathbf{63} \oplus 2\cdot\mathbf{720} \oplus 1\cdot\mathbf{945} \oplus 1\cdot\overline{\mathbf{945}} \oplus 1\cdot\mathbf{2352}$

TABLE XXII. SU(8)$_1$ WZW model – Tower of states starting from ☐ (resp. ⊟ by conjugation of all IRREPs).

L_0	Order	Irreps / Multiplicities
0	$q^{7/16}$	**1** ☐ **8**
1	$q^{23/16}$	**1** ☐ **8** ⊕ **1** ⊞ **216**
2	$q^{39/16}$	**2** ☐ **8** ⊕ **2** ⊞ **216** ⊕ **1** ⊟ **280** ⊕ **1** ⊟ **1344**

TABLE XXIII. SU(8)$_1$ WZW model – Tower of states starting from ⊟ (resp. ⊟ by conjugation of all IRREPs).

L_0	Order	Irreps / Multiplicities
0	$q^{3/4}$	**1** ⊟ **28**
1	$q^{7/4}$	**1** ⊟ **28** ⊕ **1** ☐☐ **36** ⊕ **1** ⊟ **420**
2	$q^{11/4}$	**3** ⊟ **28** ⊕ **1** ☐☐ **36** ⊕ **2** ⊟ **420** ⊕ **1** ⊟ **1280** ⊕ **1** ⊟ **1512**

TABLE XXIV. SU(8)$_1$ WZW model – Tower of states starting from ☐ (resp. ☐ by conjugation of all IRREPs).
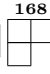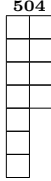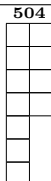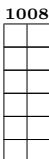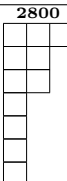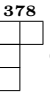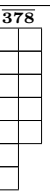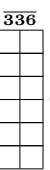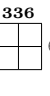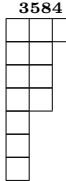

TABLE XXV. SU(8)$_1$ WZW model – Tower of states starting from ☐.

FIG. 17. Energy difference between the ground state of the antisymmetric IRREP $aIR_N(r_0)$ and the completely symmetric (ferromagnetic) state for $\theta = \pi/4$, $N = 4$ (red) and $N = 8$ (blue), $\phi = \pi/2$ (filled symbols) and $\phi = \pi$ (open symbols). In all cases, the energy difference scales approximately linearly with N_s, revealing a macroscopic energy difference.

Appendix D: Notes on finite size effects in ED of periodic clusters

1. Antisymmetric vs completely symmetric IRREPS

In the range $\phi \in [0, \pi]$ both J_1 and J_2 couplings are antiferromagnetic but the amplitude J_R of the (real) 3-site permutation changes sign, from positive to negative, at $\phi = \pi/2$. Although a negative J_R equally favors both, the completely symmetric multiplet (ferromagnetic) as well as the *completely* antisymmetric multiplet on any triangle (see App. A), on finite (periodic) clusters (with $N_s > N$), it strongly favors the ferromagnetic state with respect to the antisymmetric (antiferromagnetic) states of $aIR_N(r_0)$. In fact, a 3-site permutation on a triangle with $J_R < 0$ cannot accommodate the complicated sign structure of antiferromagnetic states. Note also that the energy difference is *macroscopic*, in the sense that it scales with the number of sites N_s. At $\phi = \pi/2$ where J_R vanishes and the antiferromagnetic couplings J_1 and J_2 are finite, we observe the reverse, namely a macroscopic energy penalty for the ferromagnetic state with respect to the antiferromagnetic states. This is clearly evidenced in Fig. 17, showing the energy difference $E_a(N_s) - E_F(N_s)$ vs N_s, for $\theta = \pi/4$, and $N = 4$ and $N = 8$. Then, one can argue that a transition from a spin liquid phase (or several spin liquid phases) and the ferromagnetic phase should occur between $\phi = \pi/2$ and $\phi = \pi$.

2. Finite size effects in low-energy spectra

As seen in App. App. A, for a given system size N_s (multiple of N), the spectrum of the SU(N) model includes all SU(N') spectra, $N' < N$. In the frustrated antiferromagnetic regime where a SU(N) chiral spin liquid (or a singlet cluster state) is expected, SU(M) singlets (forming a higher
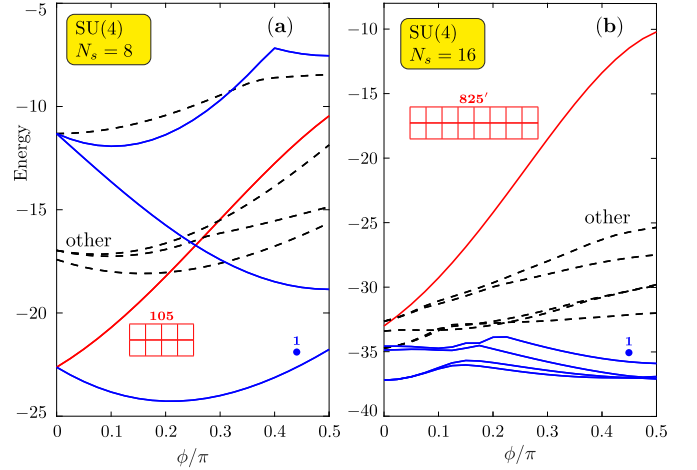
FIG. 18. Low-energy spectra of the SU(4) model computed on 8-site (a) and 16-site (b) periodic clusters at $\theta = \pi/4$, plotted vs ϕ. A few of the lowest energies of the SU(4) singlet subspace are shown (in blue) on both panels as well as the lowest energy (in red) within the subspace of the higher Casimir [4400] (or **105**) (a) and [8800] (or **825'**) (b) IRREPs, which can also be viewed as SU(2) singlets. Other lowest-energy excitations are also shown for completeness.

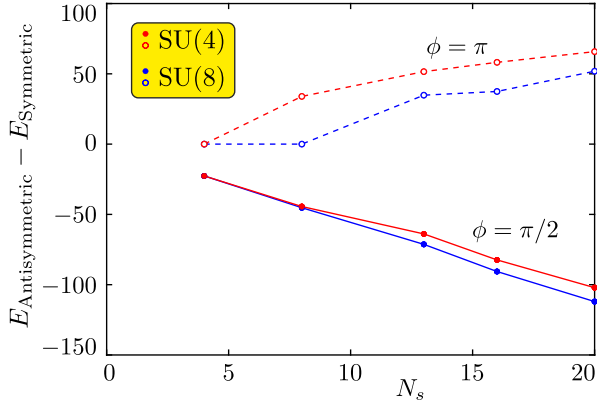quadratic Casimir SU(N) IRREP), $M < N$ also divider of N_s, may compete with the expected SU(N) singlet GS of the SU(N) model. We have observed this effect in Fig. 2 for $N = 8, 9, 10$ (with $N_s = 16, 18, 20$ and $M = 4, 6, 5$, respectively) for $\theta = \pi/4$ and small ϕ. For instance, for $N_s = 16$ and $N = 8$, the high Casimir IRREP [44440000] has energy given by Fig. 2 (c) which is smaller at $\phi = 0$ than the one of the SU(8) singlet subspace in Fig. 2 (g).

Here we argue that such a behavior is in fact a finite size effect occuring when $N_s < N^2$. To illustrate it we compare in Fig. 18 the low-energy spectra of the $N = 4$ model at $\theta = \pi/4$, versus ϕ, on 8-site and 16-site clusters. For $N_s = 8$, we observe that the lowest energies of the SU(4) singlets and those of the higher Casimir IRREP [4400] (also SU(2) singlets) are comparable. In contrast, for $N_s = 16$, a clear energy separation is seen between the lowest energy states of the higher Casimir [8800] IRREP (also SU(2) singlets) and the lowest SU(4) singlets.

Appendix E: Details on MPO–MPS implementation

This section describes how to cast a Slater determinant, $|\Psi\rangle = \prod_{k,\sigma} d_{k\sigma}^\dagger |0\rangle$, into an MPS with conserved spin symmetry. We elaborate our implementation for $N = 2$; the generalization to larger N is straightforward. For spin-1/2 fermions, the standard approach to express a single-particle operator $d_{k\sigma}^\dagger$ is to map the L-site spinful fermions onto a $2L$-site pseudospin-1/2 chain using the Jordan–Wigner transformation [67, 103, 104], namely,

$$
\begin{aligned}
c_{\ell,\uparrow}^\dagger &\to \sigma_1^z \cdots \sigma_{2\ell-2}^z \sigma_{2\ell-1}^+ \\
c_{\ell,\downarrow}^\dagger &\to \sigma_1^z \cdots \sigma_{2\ell-2}^z \sigma_{2\ell-1}^z \sigma_{2\ell}^+.
\end{aligned}
\tag{E1}
$$

And, $d^\dagger_{k\sigma} = \sum_{m,n} A_{m,n}(k) c^\dagger_{m,n,\sigma} = \sum_\ell \tilde{A}_{k\sigma,\ell} c^\dagger_{\ell\sigma}$ can be read as an MPO acting on the spin-1/2 chain

$$d^\dagger_{k\sigma} = \begin{pmatrix} 0 & 1 \end{pmatrix} \left[\prod_{\ell=1}^{2L} \begin{pmatrix} \mathbb{1}_\ell & 0 \\ \tilde{A}_{k\sigma,\ell}\sigma^+_\ell & \sigma^z_\ell \end{pmatrix} \right] \begin{pmatrix} 1 \\ 0 \end{pmatrix}. \tag{E2}$$

For our purpose, we would like to block $2\ell - 1$ and 2ℓ sites together, which leads to

$$d^\dagger_{k\sigma} = \begin{pmatrix} 0 & 1 \end{pmatrix} \left[\prod_{j=1}^{L} \begin{pmatrix} \mathbb{1}_{2j-1} \otimes \mathbb{1}_{2j} & 0 \\ \tilde{A}_{k\sigma,2j-1}\sigma^+_{2j-1} \otimes \mathbb{1}_{2j} + \tilde{A}_{k\sigma,2j}\sigma^z_{2j-1} \otimes \sigma^+_{2j} & \sigma^z_{2j-1} \otimes \sigma^z_{2j} \end{pmatrix} \right] \begin{pmatrix} 1 \\ 0 \end{pmatrix}. \tag{E3}$$

We can identify $\sigma^+_{2j-1} \otimes \mathbb{1}_{2j}$ with $c^\dagger_{j,\uparrow}$, $\sigma^z_{2j-1} \otimes \sigma^+_{2j}$ with $c^\dagger_{j,\downarrow}$, and $F_j = \sigma^z_{2j-1} \otimes \sigma^z_{2j}$ with the parity operator to account for anticommutation of different sites. In fact, we can always write the MPO in this spinful fermion basis, regardless of the number of fermion species, i.e.,

$$d^\dagger_{k\sigma} = \begin{pmatrix} 0 & 1 \end{pmatrix} \left[\prod_{j=1}^{L} \begin{pmatrix} \mathbb{I} & 0 \\ \tilde{A}_{k\sigma,j}c^\dagger_\sigma & F \end{pmatrix} \right] \begin{pmatrix} 1 \\ 0 \end{pmatrix}. \tag{E4}$$

This facilitates working with U(1) or SU(N) spin symmetry as each tensor index can be associated with a specific quantum number (see Fig. 19). With U(1) spin symmetry, one can fuse the virtual indices at boundaries of each pair of MPOs to be $S_z = 0$ (see Fig. 20), the resulting MPS $|\Psi\rangle$ also has $S_z = 0$. In the same way, one can easily impose SU(2) spin symmetry to target spin-singlet states, provided an efficient tensor network implementation to handle Clebsch-Gordan coefficients [82, 105–107]. We use QSpace for this purpose [82, 83].
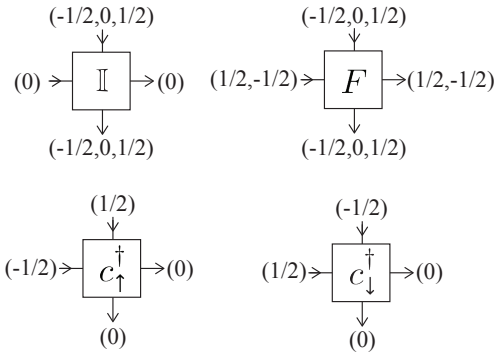
FIG. 19. Graphical representation of MPO matrix elements with U(1) spin symmetry for spin-1/2 fermions. Numbers in brackets indicate the possible values of S_z quantum numbers, $0, -1/2$ and $1/2$ representing the $|\rangle$, $|\downarrow\rangle$ and $|\uparrow\rangle$ at each physical site, respectively. Double occupancy, $|\uparrow\downarrow\rangle$, is excluded.

In Fig. 21 **(b,c)**, we plot the ESs obtained from the parton construction on a 4×12 cylinder. This demonstrates the efficacy of our parton approach, as we are able to prepare trial states in distinct topological sectors for iDMRG using a relatively small size cylinder. Additionally, imposing SU(2) symmetry constraint leads to an intriguing consequence: if the state is in the topologically nontrivial sector, there are multiple degenerate branches in the ES (see Fig. 21(c)). This
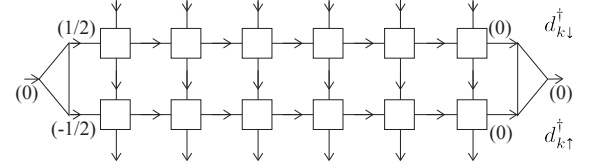
FIG. 20. Graphical representation of fusing edge virtual indices of 2 MPOs, $d^\dagger_{k\uparrow}$ and $d^\dagger_{k\downarrow}$.

has also been observed in the SU(2) iPEPS simulations previously [44, 52, 90], and was attributed to the so-called "dressed mirror symmetry" within the virtual degrees of freedom [90]. The parton approach offers a more direct understanding — the degeneracy equals to the number of parton states required to form a singlet superposition state.
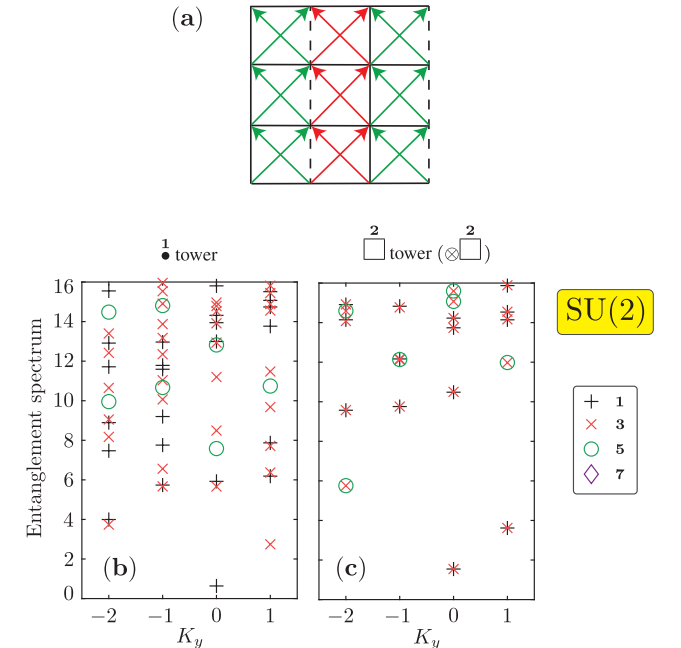
FIG. 21. **(a)** Illustration of the parton Hamiltonian of the SU(2) CSL. The phase of nearest neighbor hopping is 0 (π) along the solid (dashed) edges. The phase of next-nearest-neighbor hopping is $\pi/2$ $(-\pi/2)$ along the green (red) arrows. **(b,c)** The entanglement spectra on a 4×12 cylinder for the parton wave function.

Appendix F: Modified WZW SU(N)$_1$ chiral towers of states

We list here, for $N = 3$ and 4, the predicted ToS corresponding to the SU(N) DMRG cylinders investigated and discussed in the main text.

[1] Grégoire Misguich and Claire Lhuillier, "Two-dimensional quantum antiferromagnets," in Frustrated Spin Systems, edited by H. T. Diep (World Scientific, 2005) pp. 229–306.

[2] Lucile Savary and Leon Balents, "Quantum spin liquids: a review," Reports on Progress in Physics **80**, 016502 (2016).

[3] Yi Zhou, Kazushi Kanoda, and Tai-Kai Ng, "Quantum spin liquid states," Rev. Mod. Phys. **89**, 025003 (2017).

[4] X. G. Wen, "Topological orders in rigid states," International Journal of Modern Physics B **04**, 239–271 (1990).

[5] Didier Poilblanc, Norbert Schuch, David Pérez-García, and J. Ignacio Cirac, "Topological and entanglement properties of resonating valence bond wave functions," Phys. Rev. B **86**, 014404 (2012).

[6] V. Kalmeyer and R. B. Laughlin, "Equivalence of the resonating-valence-bond and fractional quantum Hall states," Phys. Rev. Lett. **59**, 2095–2098 (1987).

[7] Vadim Kalmeyer and R. B. Laughlin, "Theory of the spin liquid state of the heisenberg antiferromagnet," Phys. Rev. B **39**, 11879–11899 (1989).

[8] R. B. Laughlin, "Spin hamiltonian for which quantum hall wavefunction is exact," Annals of Physics **191**, 163–202 (1989).

[9] X. G. Wen, Frank Wilczek, and A. Zee, "Chiral spin states and superconductivity," Phys. Rev. B **39**, 11413–11423 (1989).

[10] R. B. Laughlin and Z. Zou, "Properties of the chiral-spin-liquid state," Phys. Rev. B **41**, 664–687 (1990).

[11] Xiao-Gang Wen, "Quantum orders and symmetric spin liquids," Phys. Rev. B **65**, 165113 (2002).

[12] D. C. Tsui, H. L. Stormer, and A. C. Gossard, "Two-dimensional magnetotransport in the extreme quantum limit," Phys. Rev. Lett. **48**, 1559–1562 (1982).

[13] B. I. Halperin, "Statistics of quasiparticles and the hierarchy of fractional quantized Hall states," Phys. Rev. Lett. **52**, 1583–1586 (1984).

[14] X. G. Wen, "Gapless boundary excitations in the quantum Hall states and in the chiral spin states," Phys. Rev. B **43**, 11025–11036 (1991).

[15] Darrell F. Schroeter, Eliot Kapit, Ronny Thomale, and Martin Greiter, "Spin hamiltonian for which the chiral spin liquid is the exact ground state," Phys. Rev. Lett. **99**, 097202 (2007).

[16] Ronny Thomale, Eliot Kapit, Darrell F. Schroeter, and Martin Greiter, "Parent hamiltonian for the chiral spin liquid," Phys. Rev. B **80**, 104406 (2009).

[17] Anne E. B. Nielsen, J. Ignacio Cirac, and Germán Sierra, "Laughlin spin-liquid states on lattices obtained from conformal field theory," Phys. Rev. Lett. **108**, 257206 (2012).

[18] Martin Greiter, Darrell F. Schroeter, and Ronny Thomale, "Parent Hamiltonian for the non-Abelian chiral spin liquid," Phys. Rev. B **89**, 165125 (2014).

[19] B. Bauer, L. Cincio, B.P. Keller, M. Dolfi, G. Vidal, S. Trebst, and A. W. W. Ludwig, "Chiral spin liquid and emergent anyons in a kagome lattice Mott insulator," Nature Communications **5**, 5137 (2014).

[20] Anne E. B. Nielsen, Germán Sierra, and J. Ignacio Cirac, "Local models of fractional quantum Hall states in lattices and physical implementation," Nature Communications **4**, 2864 (2013).

[21] Alexander Wietek and Andreas M. Läuchli, "Chiral spin liquid and quantum criticality in extended $s = \frac{1}{2}$ Heisenberg models on the triangular lattice," Phys. Rev. B **95**, 035141 (2017).

[22] Shou-Shu Gong, W. Zhu, J.-X. Zhu, D. N. Sheng, and Kun Yang, "Global phase diagram and quantum spin liquids in a spin-$\frac{1}{2}$ triangular antiferromagnet," Phys. Rev. B **96**, 075116 (2017).

[23] A.Yu. Kitaev, "Fault-tolerant quantum computation by anyons," Annals of Physics **303**, 2 – 30 (2003).

[24] Alexei Kitaev, "Anyons in an exactly solved model and beyond," Annals of Physics **321**, 2 – 111 (2006).

[25] Hong Yao and Steven A. Kivelson, "Exact chiral spin liquid with non-abelian anyons," Phys. Rev. Lett. **99**, 247203 (2007).

[26] Martin Greiter and Ronny Thomale, "Non-abelian statistics in a quantum antiferromagnet," Phys. Rev. Lett. **102**, 207203 (2009).

[27] A. V. Gorshkov, M. Hermele, V. Gurarie, C. Xu, P. S. Julienne, J. Ye, P. Zoller, E. Demler, M. D. Lukin, and A. M. Rey, "Two-orbital SU(N) magnetism with ultracold alkaline-earth atoms," Nature Physics **6**, 289–295 (2010).

[28] Michael Hermele, Victor Gurarie, and Ana Maria Rey, "Mott insulators of ultracold fermionic alkaline earth atoms: Underconstrained magnetism and chiral spin liquid," Phys. Rev. Lett. **103**, 135301 (2009).

[29] Pierre Nataf, Miklós Lajkó, Alexander Wietek, Karlo Penc, Frédéric Mila, and Andreas M. Läuchli, "Chiral spin liquids in triangular-lattice SU(N) fermionic mott insulators with artificial gauge fields," Phys. Rev. Lett. **117**, 167202 (2016).

[30] Gang Chen, Kaden R. A. Hazzard, Ana Maria Rey, and Michael Hermele, "Synthetic-gauge-field stabilization of the chiral-spin-liquid phase," Phys. Rev. A **93**, 061601 (2016).

[31] Yin-Chen He, D. N. Sheng, and Yan Chen, "Chiral spin liquid in a frustrated anisotropic Kagome Heisenberg model," Phys. Rev. Lett. **112**, 137202 (2014).

[32] Shou-Shu Gong, W. Zhu, and D. N. Sheng, "Emergent chiral spin liquid: Fractional quantum Hall effect in a kagome Heisenberg model," Scientific Reports **4**, 6317 (2014).

[33] Alexander Wietek, Antoine Sterdyniak, and Andreas M. Läuchli, "Nature of chiral spin liquids on the kagome lattice," Phys. Rev. B **92**, 125122 (2015).

[34] C. Boos, C. J. Ganahl, M. Lajkó, P. Nataf, A. M. Läuchli, K. Penc, K. P. Schmidt, and F. Mila, "Time-reversal symmetry breaking abelian chiral spin liquid in mott phases of three-component fermions on the triangular lattice," Phys. Rev. Research **2**, 023098 (2020).

[35] G. Pagano, M. Mancini, G. Cappellini, and et al., "A one-dimensional liquid of fermions with tunable spin," Nature Physics **10**, 198–201 (2014).

[36] Ya-Hui Zhang, D. N. Sheng, and Ashvin Vishwanath, "An $su(4)$ chiral spin liquid and quantized dipole hall effect in

moir bilayers," (2021), arXiv:2103.09825 [cond-mat.str-el].

[37] F. Verstraete and J. I. Cirac, "Renormalization algorithms for Quantum-Many Body Systems in two and higher dimensions," arXiv e-prints , cond-mat/0407066 (2004), arXiv:cond-mat/0407066 [cond-mat.str-el].

[38] H. J. Liao, Z. Y. Xie, J. Chen, Z. Y. Liu, H. D. Xie, R. Z. Huang, B. Normand, and T. Xiang, "Gapless spin-liquid ground state in the $s = 1/2$ Kagome antiferromagnet," Phys. Rev. Lett. **118**, 137202 (2017).

[39] Hyun-Yong Lee, Ryui Kaneko, Tsuyoshi Okubo, and Naoki Kawashima, "Gapless Kitaev spin liquid to classical string gas through tensor networks," Phys. Rev. Lett. **123**, 087203 (2019).

[40] Wen-Yuan Liu, Shou-Shu Gong, Yu-Bin Li, Didier Poilblanc, Wei-Qiang Chen, and Zheng-Cheng Gu, "Gapless quantum spin liquid and global phase diagram of the spin-1/2 J_1-J_2 square antiferromagnetic Heisenberg model," (2020), arXiv:2009.01821 [cond-mat.str-el].

[41] Norbert Schuch, J. Ignacio Cirac, and David Pérez-García, "PEPS as ground states: Degeneracy and topology," Annals of Physics **325**, 2153–2192 (2010).

[42] Norbert Schuch, Didier Poilblanc, J. Ignacio Cirac, and David Pérez-García, "Resonating valence bond states in the PEPS formalism," Physical Review B **86**, 115108 (2012).

[43] Ji-Yao Chen and Didier Poilblanc, "Topological $\mathbb{Z}_2$ resonating-valence-bond spin liquid on the square lattice," Phys. Rev. B **97**, 161107 (2018).

[44] Didier Poilblanc, J. Ignacio Cirac, and Norbert Schuch, "Chiral topological spin liquids with projected entangled pair states," Phys. Rev. B **91**, 224431 (2015).

[45] Ji-Yao Chen, Laurens Vanderstraeten, Sylvain Capponi, and Didier Poilblanc, "Non-abelian chiral spin liquid in a quantum antiferromagnet revealed by an iPEPS study," Phys. Rev. B **98**, 184409 (2018).

[46] Philippe Francesco, Pierre Mathieu, and David Sénéchal, Conformal Field Theory (Springer-Verlag New York, 1997).

[47] Ji-Yao Chen, Sylvain Capponi, Alexander Wietek, Matthieu Mambrini, Norbert Schuch, and Didier Poilblanc, "SU(3)$_1$ chiral spin liquid on the square lattice: A view from symmetric projected entangled pair states," Phys. Rev. Lett. **125**, 017201 (2020).

[48] Didier Poilblanc, "Investigation of the chiral antiferromagnetic Heisenberg model using projected entangled pair states," Phys. Rev. B **96**, 121118 (2017).

[49] The chiral spin liquid phase should also exist away from $J_2 = J_1/2$, due to its gapped nature.

[50] This can be extended to all fundamental IRREPs of SU(N): $P_{ij} = \mathbf{J}_i \cdot \mathbf{J}_j + \frac{1}{N}$, where J^α are the generators defined in Eq. (C1) of App. C. Note, the usual SU(2) spin operators are given by $\mathbf{S} = (1/\sqrt{2})\mathbf{J}$.

[51] This decomposition holds only for $N = 2$ (in the fundamental representation).

[52] Didier Poilblanc, Norbert Schuch, and Ian Affleck, "SU(2)$_1$ chiral edge modes of a critical spin liquid," Phys. Rev. B **93**, 174414 (2016).

[53] Pierre Nataf and Frédéric Mila, "Exact diagonalization of Heisenberg SU(n) models," Phys. Rev. Lett. **113**, 127204 (2014).

[54] Kianna Wan, Pierre Nataf, and Frédéric Mila, "Exact diagonalization of SU(N) Heisenberg and Affleck-Kennedy-Lieb-Tasaki chains using the full SU(N) symmetry," Phys. Rev. B **96**, 115159 (2017).

[55] Arne Alex, Matthias Kalus, Alan Huckleberry, and Jan von Delft, "A numerical algorithm for the explicit calculation of SU(N) and SL(n, $\mathbb{C}$)sl(n,c) ClebschGordan coefficients," Journal of Mathematical Physics **52**, 023507 (2011).

[56] Both states are translationally invariant and have different ± 1 characters under $\pi/2$-rotation, for C_4-symmetric clusters.

[57] R. Haghshenas, Wang-Wei Lan, Shou-Shu Gong, and D. N. Sheng, "Quantum phase diagram of spin-1 J_1-J_2 Heisenberg model on the square lattice: An infinite projected entangled-pair state and density matrix renormalization group study," Phys. Rev. B **97**, 184436 (2018).

[58] Ji-Yao Chen, Sylvain Capponi, and Didier Poilblanc, "Discrete lattice symmetry breaking in a two-dimensional frustrated spin-1 Heisenberg model," Phys. Rev. B **98**, 045106 (2018).

[59] Benoit Estienne and B. Andrei Bernevig, "Spin-singlet quantum hall states and jack polynomials with a prescribed symmetry," Nucl. Phys. B **857**, 185 – 206 (2012).

[60] A. Sterdyniak, C. Repellin, B. Andrei Bernevig, and N. Regnault, "Series of abelian and non-abelian states in $c > 1$ fractional chern insulators," Phys. Rev. B **87**, 205137 (2013).

[61] Yi Zhang, Tarun Grover, Ari Turner, Masaki Oshikawa, and Ashvin Vishwanath, "Quasiparticle statistics and braiding from ground-state entanglement," Phys. Rev. B **85**, 235151 (2012).

[62] A. A. Abrikosov, "Electron scattering on magnetic impurities in metals and anomalous resistivity effects," Physics Physique Fizika **2**, 5–20 (1965).

[63] X. G. Wen, "Non-abelian statistics in the fractional quantum hall states," Phys. Rev. Lett. **66**, 802–805 (1991).

[64] Assa Auerbach, "Interacting electrons and quantum magnetism," (Springer, Berlin, 1998).

[65] Hong-Hao Tu, Yi Zhang, and Xiao-Liang Qi, "Momentum polarization: An entanglement measure of topological spin and chiral central charge," Phys. Rev. B **88**, 195412 (2013).

[66] Jia-Wei Mei and Xiao-Gang Wen, "Modular matrices from universal wave-function overlaps in Gutzwiller-projected parton wave functions," Phys. Rev. B **91**, 125123 (2015).

[67] Ying-Hai Wu, Lei Wang, and Hong-Hao Tu, "Tensor network representations of parton wave functions," Phys. Rev. Lett. **124**, 246401 (2020).

[68] Hui Li and F. D. M. Haldane, "Entanglement spectrum as a generalization of entanglement entropy: Identification of topological order in non-abelian fractional quantum hall effect states," Phys. Rev. Lett. **101**, 010504 (2008).

[69] Hui-Ke Jin, Hong-Hao Tu, and Yi Zhou, "Density matrix renormalization group boosted by gutzwiller projected wave functions," Phys. Rev. B **104**, L020409 (2021).

[70] W. Li, A. Weichselbaum, and J. von Delft, "Identifying symmetry-protected topological order by entanglement entropy," Phys. Rev. B **88**, 245121–245129 (2013).

[71] A.Yu. Kitaev, "Fault-tolerant quantum computation by anyons," Annals of Physics **303**, 2 – 30 (2003).

[72] L. Cincio and G. Vidal, "Characterizing topological order by studying the ground states on an infinite cylinder," Phys. Rev. Lett. **110**, 067208 (2013); "Characterizing topological order by studying the ground states on an infinite cylinder," arXiv:1208.2623 [cond-mat.str-el] .

[73] Simeng Yan, David A. Huse, and Steven R. White, "Spin-liquid ground state of the s = 1/2 kagome heisenberg antiferromagnet," Science **332**, 1173–1176 (2011).

[74] Michael P. Zaletel, Roger S. K. Mong, and Frank Pollmann, "Topological characterization of fractional quantum hall ground states from microscopic hamiltonians," Phys. Rev. Lett. **110**, 236801 (2013).

[75] S. N. Saadatmand and I. P. McCulloch, "Symmetry fractionalization in the topological phase of the spin-$\frac{1}{2}$ J_1-J_2 triangular Heisenberg model," Phys. Rev. B **94**, 121111 (2016).

[76] Shijie Hu, W. Zhu, Sebastian Eggert, and Yin-Chen He, "Dirac spin liquid on the spin-1/2 triangular Heisenberg antiferromagnet," Phys. Rev. Lett. **123**, 207203 (2019).

[77] Aaron Szasz, Johannes Motruk, Michael P. Zaletel, and Joel E. Moore, "Chiral spin liquid phase of the triangular lattice Hubbard model: A density matrix renormalization group study," Phys. Rev. X **10**, 021042 (2020).

[78] For SU(N)$_1$ CSL all topological sectors can be obtained in this way. However, for some topological phases, other types of anyon sectors can appear, such as a "defect line" cutting along the x direction. This is also very common and appears in, e.g., $\mathbb{Z}_2$ [5] and Ising topological phases. Then, adopting tailored boundaries in DMRG is not sufficient to detect such topological sectors.

[79] Steven R. White, "Density matrix formulation for quantum renormalization groups," Phys. Rev. Lett. **69**, 2863–2866 (1992).

[80] I. P. McCulloch, "Infinite size density matrix renormalization group, revisited," arXiv:0804.2509 [cond-mat.str-el] .

[81] This is similar to the AKLT state with periodic boundary conditions, which has four-fold degeneracy in the entanglement spectrum rather than the two-fold degeneracy suggested by the $D = 2$ MPS representation [70].

[82] Andreas Weichselbaum, "Non-abelian symmetries in tensor networks: A quantum symmetry space approach," Annals of Physics **327**, 2972 – 3047 (2012).

[83] Andreas Weichselbaum, "X-symbols for non-abelian symmetries in tensor networks," Phys. Rev. Research **2**, 023385 (2020).

[84] To describe non-Abelian SU(N)$_k$ CSL, $k > 1$, we speculate that one should include all IRREPS in $\mathcal{V}$ with up to k columns, consistently with the SU(2)$_2$ case [45].

[85] Matthieu Mambrini, Román Orús, and Didier Poilblanc, "Systematic construction of spin liquids on the square lattice from tensor networks with SU(2) symmetry," Phys. Rev. B **94**, 205124 (2016).

[86] Tomotoshi Nishino and Kouichi Okunishi, "Corner transfer matrix renormalization group method," Journal of the Physical Society of Japan **65**, 891–894 (1996).

[87] Román Orús and Guifré Vidal, "Simulation of two-dimensional quantum systems on an infinite lattice revisited: Corner transfer matrix for tensor contraction," Physical Review B **80**, 094403 (2009).

[88] Didier Poilblanc and Matthieu Mambrini, "Quantum critical phase with infinite projected entangled paired states," Phys. Rev. B **96**, 014414 (2017).

[89] J. Ignacio Cirac, Didier Poilblanc, Norbert Schuch, and Frank Verstraete, "Entanglement spectrum and boundary theories with projected entangled-pair states," Phys. Rev. B **83**, 245134 (2011).

[90] Anna Hackenbroich, Antoine Sterdyniak, and Norbert Schuch, "Interplay of SU(2), point group, and translational symmetry for projected entangled pair states: Application to a chiral spin liquid," Phys. Rev. B **98**, 085151 (2018).

[91] J. Dubail and N. Read, "Tensor network trial states for chiral topological phases in two dimensions and a no-go theorem in any dimension," Phys. Rev. B **92**, 205307 (2015).

[92] Olivier Gauthé, Sylvain Capponi, Matthieu Mambrini, and Didier Poilblanc, "Quantum spin liquid phases in the bilinear-biquadratic two-SU(4)-fermion hamiltonian on the square lattice," Phys. Rev. B **101**, 205144 (2020).

[93] A. Weichselbaum, S. Capponi, P. Lecheminant, A. M. Tsvelik, and A. M. Läuchli, "Unified phase diagram of antiferromagnetic su(n) spin ladders," Phys. Rev. B **98**, 085104 (2018).

[94] B. I. Halperin, "Theory of the quantized hall conductance," Helv. Phys. Acta **56**, 75 (1983).

[95] Hong-Hao Tu, A. E. B. Nielsen, and Germán Sierra, "Quantum spin models for the SU(n)$_1$ Wess-Zumino-Witten model," Nucl. Phys. B **886**, 328 (2014).

[96] Roberto Bondesan and Thomas Quella, "Infinite matrix product states for long-range SU(N) spin models," Nucl. Phys. B **886**, 483 (2014).

[97] N. Regnault and B. Andrei Bernevig, "Fractional Chern insulator," Phys. Rev. X **1**, 021014 (2011).

[98] B. Andrei Bernevig and N. Regnault, "Emergent many-body translational symmetries of Abelian and non-Abelian fractionally filled topological insulators," Phys. Rev. B **85**, 075128 (2012).

[99] H. Georgi, Lie Algebras in Particle Physics (Perseus Books, 1999).

[100] P. Goddard and D. Olive, "Kac-Moody and Virasoro algebras in relation to quantum physics," Int. J. Mod. Phys. A **1**, 303–414 (1986).

[101] V. G. Knizhnik and A. B. Zamolodchikov, "Current algebra and Wess-Zumino model in two dimensions," Nucl. Phys. B **247**, 83–103 (1984).

[102] P. Ginsparg, "Applied conformal field theory," in Fields, Strings and Critical Phenomena, edited by E. Brézin and J. Zinn-Justin, Les Houches summer school (North-Holland, 1988).

[103] Hui-Ke Jin, Hong-Hao Tu, and Yi Zhou, "Efficient tensor network representation for Gutzwiller projected states of paired fermions," Phys. Rev. B **101**, 165135 (2020).

[104] Gabriel Petrica, Bo-Xiao Zheng, Garnet Kin-Lic Chan, and Bryan K. Clark, "Finite and infinite matrix product states for gutzwiller projected mean-field wave functions," Phys. Rev. B **103**, 125161 (2021).

[105] Sukhwinder Singh and Guifre Vidal, "Tensor network states and algorithms in the presence of a global su(2) symmetry," Phys. Rev. B **86**, 195114 (2012).

[106] Claudius Hubig, "Abelian and non-abelian symmetries in infinite projected entangled pair states," SciPost Phys. **5**, 47 (2018).

[107] Philipp Schmoll, Sukhbinder Singh, Matteo Rizzi, and Romn Ors, "A programming guide for tensor networks with global SU(2) symmetry," Annals of Physics **419**, 168232 (2020).

TABLE XXVI. SU(3)$_1$ WZW model – The direct product of the conformal tower of the $\tiny\square$ **3** primary (left - see Table VII in App. C) with $\tiny\square$ **$\bar{3}$** gives a new tower (right) with a tripling of the number of states in each Virasoro level indexed by L_0.

L_0	**3** tower			$\longrightarrow$	**3** tower $\otimes$ **$\bar{3}$**			
0	**1** $\square$ **3**				**1** $\bullet$ $\oplus$ **1** **8**			
1	**1** $\square$ **3** $\oplus$ **1** **$\bar{6}$**				**1** $\bullet$ $\oplus$ **2** **8** $\oplus$ **1** **$\overline{10}$**			
2	**2** $\square$ **3** $\oplus$ **1** **$\bar{6}$** $\oplus$ **1** **15**				**2** $\bullet$ $\oplus$ **4** **8** $\oplus$ **1** **10** $\oplus$ **1** **$\overline{10}$** $\oplus$ **1** **27**			
3	**3** $\square$ **3** $\oplus$ **3** **$\bar{6}$** $\oplus$ **2** **15**				**3** $\bullet$ $\oplus$ **8** **8** $\oplus$ **2** **10** $\oplus$ **3** **$\overline{10}$** $\oplus$ **2** **27**			

TABLE XXVII. SU(4)$_1$ WZW model – The direct product of the conformal tower of the $\tiny\square$ **4** primary (left - see Table IX in App. C) with $\tiny\square$ **$\bar{4}$** gives a new tower (right) with a quadrupling of the number of states in each Virasoro level indexed by L_0.

L_0	**4** tower				$\longrightarrow$	**4** tower $\otimes$ **$\bar{4}$**				
0	**1** $\square$ **4**					**1** $\bullet$ $\oplus$ **1** **15**				
1	**1** $\square$ **4** $\oplus$ **1** **20**					**1** $\bullet$ $\oplus$ **2** **15** $\oplus$ **1** **20$'$** $\oplus$ **1** **$\overline{45}$**				
2	**2** $\square$ **4** $\oplus$ **2** **20** $\oplus$ **1** **36**					**2** $\bullet$ $\oplus$ **5** **15** $\oplus$ **2** **20$'$** $\oplus$ **1** **45** $\oplus$ **2** **$\overline{45}$** $\oplus$ **1** **84**				
3	**4** $\square$ **4** $\oplus$ **1** **20$''$** $\oplus$ **4** **20** $\oplus$ **2** **36** $\oplus$ **1** **60**					**4** $\bullet$ $\oplus$ **10** **15** $\oplus$ **5** **20$'$** $\oplus$ **1** **$\overline{35}$** $\oplus$ **3** **45** $\oplus$ **5** **$\overline{45}$** $\oplus$ **2** **84** $\oplus$ **1** **175**				

TABLE XXVIII. SU(4)$_1$ WZW model – The direct product of the conformal tower of the ⬚ primary (left - see Table X in App. C) with ⬚ gives a new tower (right) with a multiplicative factor 6 of the number of states in each Virasoro level indexed by m.

L_0	**6** tower	→	**6** tower ⊗ **6**
0	**1** **6**		**1** • $\oplus$ **1** **15** $\oplus$ **1** **20′**
1	**1** **6** $\oplus$ **1** **10** $\oplus$ **1** **10̄**		**1** • $\oplus$ **3** **15** $\oplus$ **1** **20′** $\oplus$ **1** **45** $\oplus$ **1** **45̄**
2	**3** **6** $\oplus$ **1** **10** $\oplus$ **1** **10̄** $\oplus$ **1** **64**		**3** • $\oplus$ **6** **15** $\oplus$ **4** **20′** $\oplus$ **2** **45** $\oplus$ **2** **45̄** $\oplus$ **1** **84** $\oplus$ **1** **175**
3	**4** **6** $\oplus$ **3** **10** $\oplus$ **3** **10̄** $\oplus$ **3** **64**		**4** • $\oplus$ **13** **15** $\oplus$ **7** **20′** $\oplus$ **6** **45** $\oplus$ **6** **45̄** $\oplus$ **3** **84** $\oplus$ **3** **175**